CRYOSPHERIC GEOMORPHOLOGY: Dating Glacial Landforms II: radiometric techniques

Bethan J. Davies[1]*

[1]Centre for Quaternary Research, Department of Geography, Royal Holloway University of London, Egham Hill, Egham, Surrey, TW20 0EX

*Bethan.davies@rhul.ac.uk

Manuscript Code: 40050

Abstract

Numerical ages for glacial landforms are required to position palaeo ice extent at a given point in space and time. Radiometric methods, when appropriately calibrated and measured, allow intra- and inter-regional correlation and the production of large empirical datasets across varied and fragmented Quaternary deposits. This chapter focuses on radiocarbon ages for terrestrial and marine environments, cosmogenic nuclide dating (including exposure ages of bedrock and glacially transported boulders, and burial dating for glacial sediments), optically stimulated luminescence dating of glaciofluvial outwash, and Argon/Argon or Potassium/Argon dating of moraines interbedded with volcanic sequences. For each method, the key principles and concepts are outlined, sampling methodologies are discussed, calibration techniques and protocols are provided, and quality assurance protocols are suggested. All dating stratigraphies should take place within a geomorphological and sedimentological framework, and dating techniques must be used with knowledge of their key assumptions, best-practice guidelines and limitations. Combining glacial geomorphology with carefully constructed numerical age chronologies allows the timing of significant stabilisations of outlet glaciers at moraines to be characterised, whilst vertical transects down mountain ranges provide information on past rates and magnitudes of ice-mass thinning. These typically more expensive methods may be used with great effect in conjunction with archival, relative and incremental dating techniques, and with age-equivalent stratigraphic markers. This greatly increases the spatial coverage of the numerical dating methods and allows regional stratigraphies to be constructed. These data are critical if we are to understand ice mass response to the internal and external, climatic drivers of change.

Keywords

Chronology, cosmogenic nuclide, radiocarbon dating, glacial landforms, optically stimulated luminescence

Glossary

Aliquot	A sub-sample of the material being measured.
Allochthonous	Rocks that have been transported & deposited (inc. erratics, alluvial fans, gelifluction, etc.
Attenuation length (Λ)	Thickness of a material (rock, snow, ice) required to attenuate intensity of cosmic-ray flux due to scattering & energy absorption
Autochthonous	Rocks that have remained at or near site of formation
ΔR	The local variation in the marine reservoir effect from the global average of 400 years.
Dipolar	The Earth's magnetic field is dipolar, with a north and south pole.
Dose	The amount of energy stored within a crystal as a result of exposure to radiation.
Dose rate	The total radiation dose per unit time that the sample was exposed to during the burial period. Expressed as radiation dose per thousand years (Gy/ky).
Equivalent dose	The laboratory estimate of the radiation dose accumulated throughout the burial period in OSL dating of sediments.
Galactic cosmic radiation	Energetic particles, mostly of protons, originating from outer space.
Gy	Gray, SI unit of radiation dose, used in Optically Stimulated Luminescence dating. I Gy = I J kg^{-1}
IRSL	Infra-red stimulated luminescence
Inheritance	Retention of remnant cosmogenic nuclides from a previous exposure
Isotopes	Families of nuclides with the same atomic number

Marine Reservoir Effect (MRE)	The concentration of radiocarbon differs between the ocean and the atmosphere, with a 'reservoir' in the global oceans. This results in an offset in the radiocarbon age of a sample. The global average MRE is 400 years.
Muon (μ)	-ve muons: short-lived energetic lepton particles that decay quickly. Can penetrate rocks to depth.
Nuclide	Atomic species characterised by a unique number of atomic number and neutron number (e.g., ^{10}Be, which has 4 protons and 6 neutrons)
OSL	Optically stimulated luminescence
Partial bleaching	Luminescence signals of only a portion of the grains in a sample were fully zeroed prior to burial (typical of glaciofluvial environments)
Production rate	Rate at which a specific nuclide is produced from a specified element or in a mineral such as quartz. Vary spatially and temporally.
SAR	Single aliquot regenerative-dose (for OSL dating)
Spallation reaction	Nuclear reaction resulting from collision of a highly energetic secondary cosmic ray neutron of energy with a target nucleus.
Terrestrial cosmogenic nuclide	A nuclide produced by the interaction of secondary cosmic radiation with exposed target atoms in earth-surface materials.

Contents

1 Introduction

In this chapter, the focus is on the application of radiometric methods to glacial landforms. These techniques, when appropriately calibrated, provide a measured numerical age for a material, together with measured laboratory uncertainties. Radiometric methods include radiocarbon dating of organic material associated with glacial landforms, cosmogenic nuclide surface exposure ages of glacially transported boulders or ice-scoured bedrock, cosmogenic nuclide burial ages, optically stimulated luminescence (OSL) dating on glaciofluvial outwash and Argon/Argon (Ar/Ar) ages on moraines interbedded with volcanic sequences. There are other methodologies available (e.g. U/Th dating), but they are infrequently applied to glacial landforms and so are not discussed here.

Radiometric methodologies such as radiocarbon dating rely on the radioactive properties of particular unstable isotopes (Lowe and Walker, 2014). These radioactive isotopes undergo a spontaneous change in organisation at an atomic level to achieve a more stable form. This process of radioactive decay is time-dependent; if the rate of decay is known, then the age of the host sediments can be determined. Other techniques, such as cosmogenic nuclide analysis, rely on the *in situ* generation of new isotopes, such as ^{10}Be. For radiometric methodologies, most measurements are undertaken by costly Accelerator Mass Spectrometry (AMS), and the selection of appropriate material is critical. A detailed understanding of morphostratigraphy and relative and incremental dating techniques such as Schmidt Hammer testing or lichenometry, alongside geomorphological mapping, can inform a dating strategy and ensure the optimum samples are taken for radiometric dating.

These radiometric dating tools have enabled the development of large datasets of numerical ages for glacial landforms, and have facilitated intra- and inter-regional correlation (Kirkbride and Winkler, 2012). The varied and fragmentary nature of Quaternary deposits, which impedes correlation on the basis of fossil content, lithology or structure, numerical ages have formed the basis for most regional correlations (e.g., Davies et al., 2020; Kirkbride and Winkler, 2012). These numerical ages have allowed glacial landforms to increasingly be used as a proxy for global and regional climatic patterns over timescales of 100 to >100,000 years (e.g., Kaplan et al., 2020; Kelley et al., 2014; Reynhout et al., 2019) and have formed the basis of new regional empirical datasets that compile data to generate new understandings of past ice sheet dynamics (Batchelor et al., 2019; Bentley et al., 2014; Dalton et al., 2020; Davies et al., 2020; Hughes et al., 2016; Larter et al., 2014; Ó Cofaigh et al., 2014).

2 Radiocarbon ages

2.1 Introduction to radiocarbon

Radiocarbon dating was developed in the 1940s (Libby, 1961, 1955), and transformed our understanding of the timing of events and rates of change as one of the most widely applied techniques for dating Quaternary environments. Over Quaternary timescales, radiocarbon dating is widely applied and relies on the principal of radioactive decay, and has been widely reviewed (Alves et al., 2018; Briner, 2011; Burr, 2013; Hatté and Jull, 2013; Jull, 2018; Lowe and Walker, 2014). It has been widely applied to understand deglacial chronologies in North America (Dalton et al., 2020; Dyke et al., 2003), Patagonia (Denton et al., 1999; Moreno et al., 2015; Strelin et al., 2011), Europe (Bateman et al., 2018; Dortch et al., 2016; Hughes et al.,

2011; Livingstone et al., 2015), and Antarctica (Larter et al., 2014; McKay et al., 2008; Ó Cofaigh et al., 2014; Simms et al., 2011).

Meteoric radiocarbon (^{14}C) is formed in our atmosphere by geomagnetic and solar modulation of cosmic rays, and variations in the carbon cycle. Natural radiocarbon forms in the Earth's stratosphere through the interaction of ^{14}N and neutrons produced by cosmic rays (Guilderson et al., 2005). The newly formed ^{14}C is oxidized to $^{14}CO_2$ where it enters the biosphere. Radiocarbon dating relies on the assumption that organic or inorganic materials were in equilibrium with the production of ^{14}C in the atmosphere (Jull, 2018), and that the ^{14}C in the organism will decay, converting ^{14}C back to ^{14}N through beta decay, following the death of the organism. Through this process, radiocarbon has a half-life of 5,568 years (Alves et al., 2018). Because of this relatively short half-life, radiocarbon dating has a useable range of ~300 to ~50,000 years (Briner, 2011; Guilderson et al., 2005). ^{14}C ages do not equate directly with calendar years, because ^{14}C concentration in the atmosphere varies through time due to changes in the production rate (Burr, 2013), and so require calibration with incremental datasets such as tree rings or corals (Reimer et al., 2013). Typical analytical uncertainties are ~2 to 5%, although calibration adds further uncertainty.

Convention dictates that uncalibrated ages are referred to as ^{14}C ka BP (radiocarbon age in thousands of years before 1950 AD) and calibrated ages as cal. ka BP (calibrated age in thousands of years before 1950 AD) (Alves et al., 2018; Reimer et al., 2013). Common tools for calibration include OxCal (Bronk Ramsey, 2009) or Calib (Stuiver et al., 2009). Calibrated ages are commonly presented as median ages, with an uncertainty to 1 or 2 sigma (σ). Ages should be presented in publications with all raw data needed for calibration to be updated by later researchers when new calibration curves are published.

2.2 Dating terrestrial glacial landforms using radiocarbon

Dating terrestrial glacial landforms using radiocarbon presupposes that organic material is available. In temperate terrestrial environments, this could include basal organic sediments in bogs, lakes and mires either in kettle holes associated directly with moraines, or samples from sites inside and outside ice limits, bracketing those moraine sequences (Figure 1). It could include marine or other organic sediments beneath the moraine that have been overridden (Hjort et al., 1997; McCabe et al., 2007) or material reworked into the moraine (Denton et al., 1999; Luckman et al., 2017; Strelin et al., 2011). In many cases, radiocarbon dating can be used in conjunction with other techniques, such as varve chronology, dendrochronology, lichenometry and cosmogenic nuclide dating, depending on the situation. Relating the time of organism death to the timing of landform generation requires careful stratigraphic work, and a clear understanding of whether the organic matter provides a minimum or maximum age for the glacier variability.

Radiocarbon ages are typically derived from bulk samples, microfossils samples requiring microscopy to extract, or macrofossil samples that can be visually identified and sampled (Small et al., 2017). Sedimentary sequences should have multiple radiocarbon ages taken in stratigraphic order, so that problematic materials yielding age reversals or consistent offsets can be identified and removed. In a sediment core, multiple up-core radiocarbon ages are required to confirm that sediments are in stratigraphic order and have not undergone significant disturbance. When multiple radiocarbon ages are available for the same site, the oldest date is typically most useful for dating past glaciation, if the dates are a stratigraphic sequence (Dalton et al., 2020) (Figure 1).

This approach to radiocarbon dating is widely used in palaeoenvironmental studies, but its application to dating terrestrial glacial landforms can be more challenging. In this realm, radiocarbon dating is most frequently applied to moraines, by dating sediments that comprise the moraine, sediments below and within (providing a minimum age) and above (providing a maximum age) the moraine (Figure 1). Careful stratigraphic work is required to ascertain whether the organic matter in question provides a minimum or maximum age for landform formation, and usually requires large datasets to produce robust chronologies (e.g., Denton et al., 1999; Moreno et al., 2015).

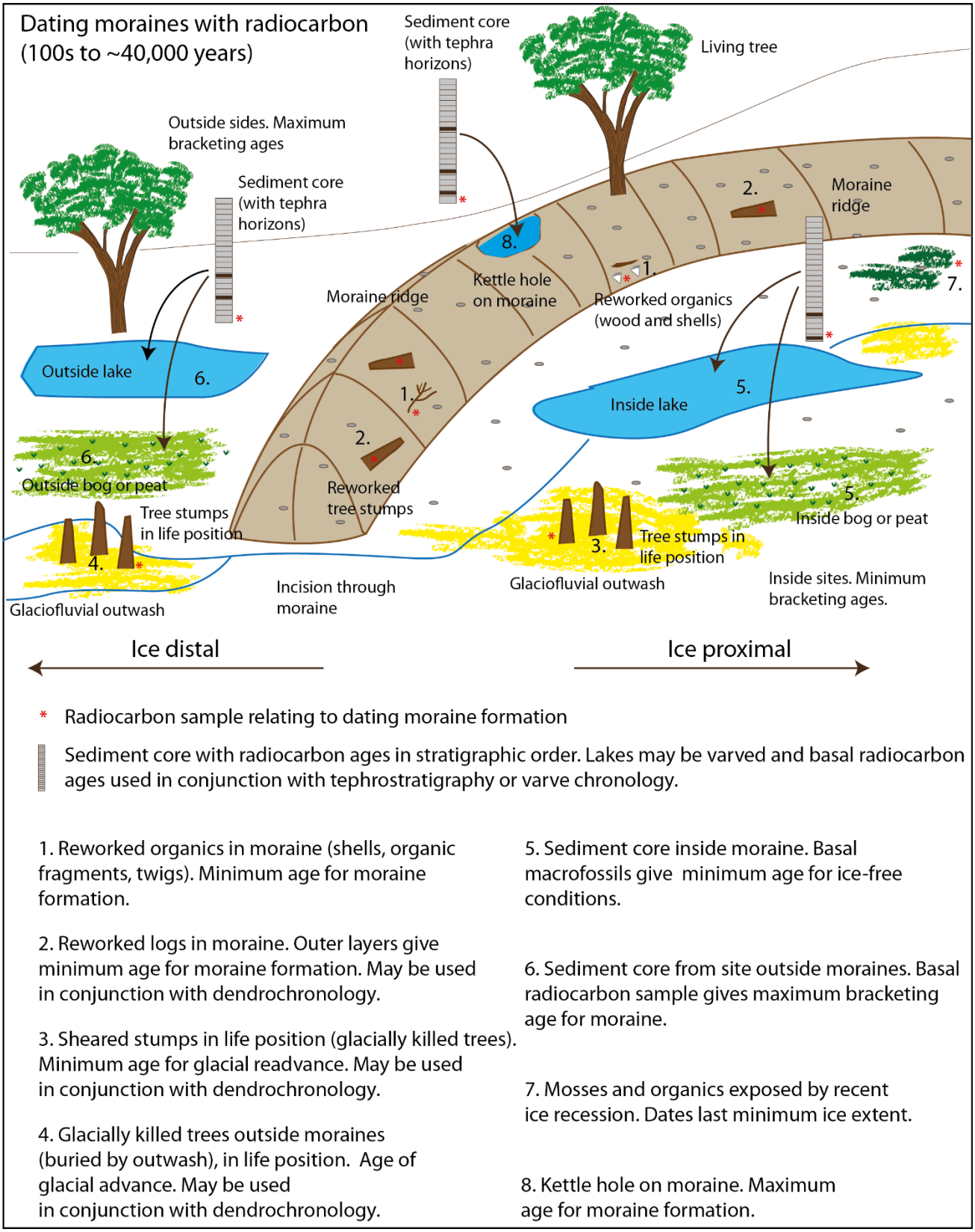

Figure 1. Cartoon illustrating techniques for dating terrestrial moraines with radiocarbon.

There are three key sources of geological uncertainty in radiocarbon ages: calibration to calendar years (see below), laboratory contamination, and site-specific geological problems (Lowe and Walker, 2000; Small et

al., 2017). Site-specific geological issues include processes, other than radioactive decay, that influence the $^{14}C/^{12}C$ ratio within an organism (before or after death), or processes that result in the age of the sample not properly reflecting the age of the sedimentary archive. The $^{14}C/^{12}C$ ratio can be affected by chemical processes such as isotopic fractionation, recrystallization, contamination, or reservoir effects (Small et al., 2017).

The geological context (transport and deposition) of the sediment can affect its geological context, and thus the relative age of the organism and the sedimentary archive. This can result in aging or rejuvenation (Hatté and Jull, 2013), caused by anomalously low (aging) or high (rejuvenation) ^{14}C content in the original carbon.

Radiocarbon dating of woody material may be challenging because the radiocarbon age may be hundreds of years older than expected, especially for long-lived trees (Hatté and Jull, 2013). The tree adds wood to the outside of the trunk every year, so for older trees, the outside may have a radiocarbon age hundreds of years younger than the heartwood. Bulk woody material reworked into moraines may lack the associated data required to inform the dating strategy. It would be best to use small twigs if possible, as they can integrate at most five years and so should give more precise ages.

For bogs, mires, lake sediments etc., some studies use an age-depth model through multiple ages in a sediment core to establish an estimate for basal age (a minimum age for the onset of deglaciation at that location). This can increase confidence in the basal age, if radiocarbon ages are present in stratigraphic order. Oldest ages give an indication of the timing of the onset of organic sedimentation, but we add the significant caveat that such ages may over- or under-estimate the true onset of deglaciation given factors such as detrital contamination or undated core sections. From these environments, terrestrial plant macrofossils should be targeted for dating.

2.3 Radiocarbon dating of freshwater environments

The ^{14}C of lakes and bog waters is often depleted, resulting in an artificial aging of the waters with wide spatial variation. Hard water can affect the dating of macrofossils from freshwater environments. The radiocarbon age of fresh water (or organisms living in the water) in contact with calcium carbonate rich rocks (such as limestone) can be increased by dissolved carbonate in the water (Hatté and Jull, 2013). The limestone contains no ^{14}C, so it acts to dilute the concentration of ^{14}C in the incoming CO_2 in the water. This can affect freshwater aquatic taxa, meaning that they have anomalous ages. Algal macrofossils should, therefore, be avoided.

Freshwater taxa (ostracods, algaes, aquatic mosses) are generally not suitable for radiocarbon dating (Dalton et al., 2020; Hatté and Jull, 2013), since algae and aquatic mosses build carbon from dissolved inorganic carbon in lakes and bog waters. This, therefore, reflects the $^{14}C:^{12}C$ ratios of the water from which they grew. These aquatic taxa are therefore vulnerable to the hard water effect. They are also vulnerable to dissolved carbonate from surrounding rocks, the residence time of the bog or lake, and other factors (Hatté and Jull, 2013).

2.4 Calibration of terrestrial radiocarbon ages

Radiocarbon dating of terrestrial samples assumes that organic or inorganic materials were in equilibrium with the production of ^{14}C in the atmosphere (Jull, 2018). After death, the plant or animal is removed from

this equilibrium, and so the level of ^{14}C should decay, allowing the time of death to be calculated. Terrestrial radiocarbon ages then require subsequent calibration before they can be related to calendar years because the value of ^{14}C in the atmosphere can vary with time (Jull, 2018). Calibration using incrementally and independently dated tree rings now extends back to 13.9 cal. Ka BP (Reimer et al., 2013; Small et al., 2017); corals, speleothems, floating tree ring chronologies and lacustrine and marine sediments have extended it back further to 55,000 cal. Years BP (Fairbanks et al., 2005; Reimer et al., 2020).

There is an offset between the Northern and Southern hemispheres, with Southern Hemisphere samples being ~40 years older, due to a higher sea-air $^{14}CO_2$ flux from the larger Southern Hemisphere oceans (Hogg et al., 2013). In these studies, the value of ^{14}C through time is calibrated against tree-rings of a known age from the appropriate hemisphere (Hogg et al., 2013; McCormac et al., 2004), with a standard offset applied beyond the range of dendrochronological methods. Radiocarbon ages, therefore, require calibration using the latest datasets (Bronk Ramsey, 2009; Hogg et al., 2013; Reimer et al., 2020, 2009).

Calibration uncertainties are, therefore, controlled by the accuracy of the calibration curve (Small et al., 2017). The use of standardized calibration curves ensures that uncertainties are consistent within a dataset. Commonly used calibration curves include SHCAL13 for terrestrial samples from the Southern Hemisphere (Hogg et al., 2013), and IntCal20 and Marine20 curves for terrestrial and marine samples from the Northern Hemisphere respectively (Heaton et al., 2020; Reimer et al., 2020, 2013). Commonly used software for calibration includes OxCal (Bronk Ramsey, 2013) and CALIB (Stuiver et al., 2009).

The calibration curves have several 'age plateaus' caused by variations in atmospheric ^{14}C content. In these plateaus, the $^{14}C/^{12}C$ ratio falls to a rate equal to that of radiocarbon decay (Guilderson et al., 2005). The utility of radiocarbon dating during these plateaus is very limited. There are two plateaus associated with the Younger Dryas (11,900 to 13,000 cal. years BP), which have made it challenging to determine synchronicity of this event globally (Guilderson et al., 2005; Muscheler et al., 2008). The Hallstatt Plateau is another flattening of the calibration curve, that homogenises calibration outputs across a 300 year interval from 2400 to 2700 cal. years BP (Burley et al., 2018). These wiggles and plateaus can cause radiocarbon ages to have several plausible calibrated ages (Small et al., 2017). A careful sampling strategy with multiple ages is required to improve the calibration here. Additionally, using independent dating tools such as tephrochronology can be beneficial.

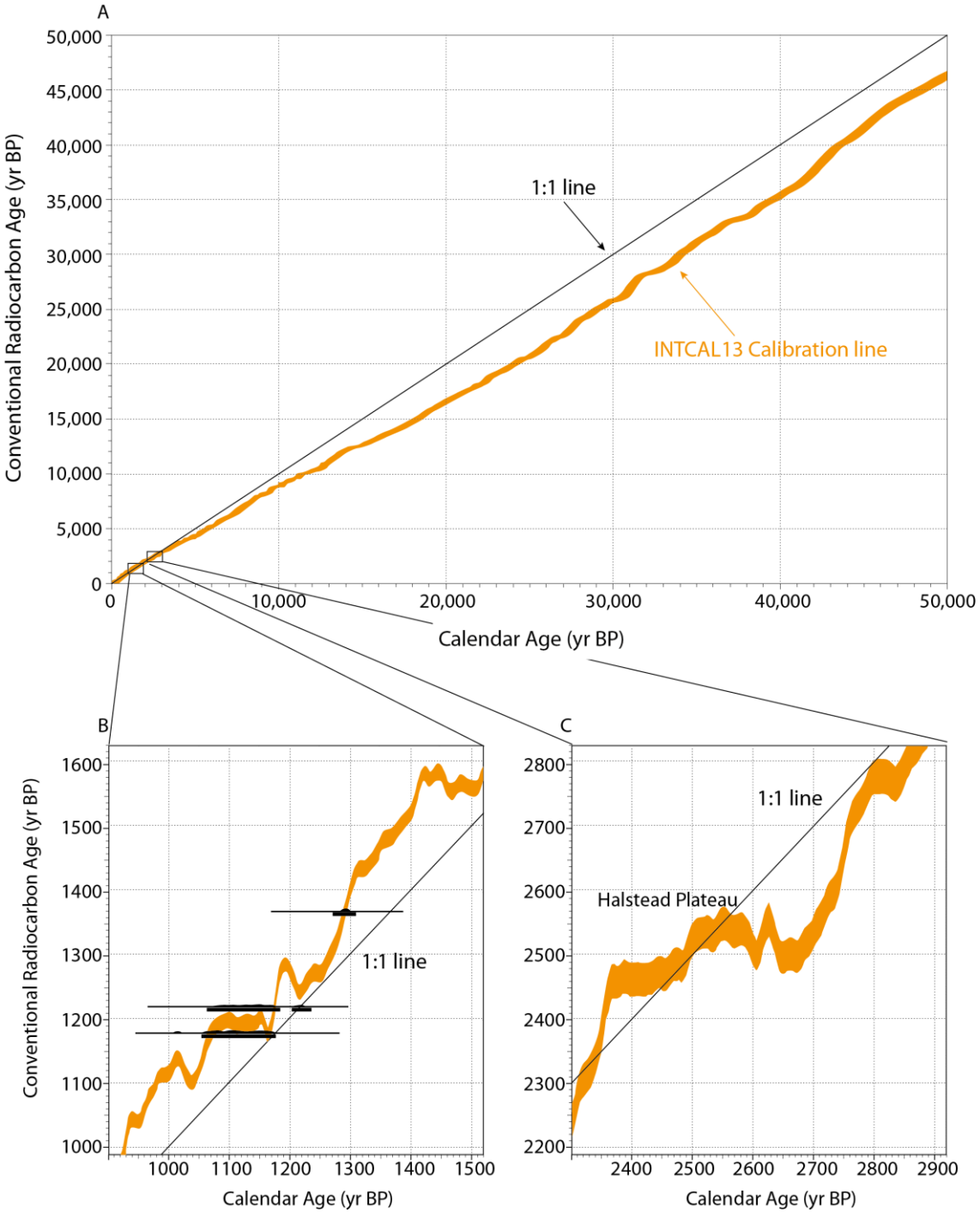

Figure 2. Radiocarbon calibration curve, with some key periods highlighted. Modified and adapted from multiple sources (Burley et al., 2018; Fairbanks et al., 2005; Guilderson et al., 2005; Reimer et al., 2013; Small et al., 2017).

2.5 Dating submarine landforms using radiocarbon

Radiocarbon dating of submarine glacial sediments has been widely applied on continental shelves in order to establish the timing and rates of ice-sheet retreat (Bentley et al., 2011; Bradwell et al., 2019; Davies et al., 2012; Heroy and Anderson, 2007; Pudsey et al., 2006; Smith et al., 2014). This is particularly widely applied

in Antarctica, where limited ice-free areas on land, combined with good access from large research ships and a well-surveyed continental shelf, make this technique particularly practical. Here, the chronology is largely derived from radiocarbon dating of bulk organic carbon or marine micro- and macro-fossils in marine sediment cores from the continental shelf and slope (Davies et al., 2012). It can be combined with multibeam swath bathymetry and seismic surveys that provide detailed images of the surface geomorphology as well as a seismic stratigraphy.

In marine settings, especially in quiescent locations on the continental shelf, a drape of organic sedimentation overlying glacial sediments and landforms (such as grounding zone wedges or morainal banks) offers the opportunity to provide a maximum age for the timing of ice recession (Kilfeather et al., 2011; Ó Cofaigh et al., 2014). Marine carbonates (single or broken bivalves) and benthic foraminifera are typically targeted for dating (Graham et al., 2017; Graham and Smith, 2012; Ó Cofaigh et al., 2019). Alternatively, ages may be obtained from bulk organic carbon in acid insoluble organic (AIO) residues (e.g., McKay et al., 2008). Here, the target sediments for dating are the “Transitional Glaciomarine Sediments” (Figure 3). These transitional glaciomarine sediments immediately over subglacial till reflect the recession of the grounding line from this point. In the ideal case, the core bottoms out in deglacial sediment, and the first samples at the boundary to glaciomarine sediments provide a minimum age for deglaciation (Ó Cofaigh et al., 2019).

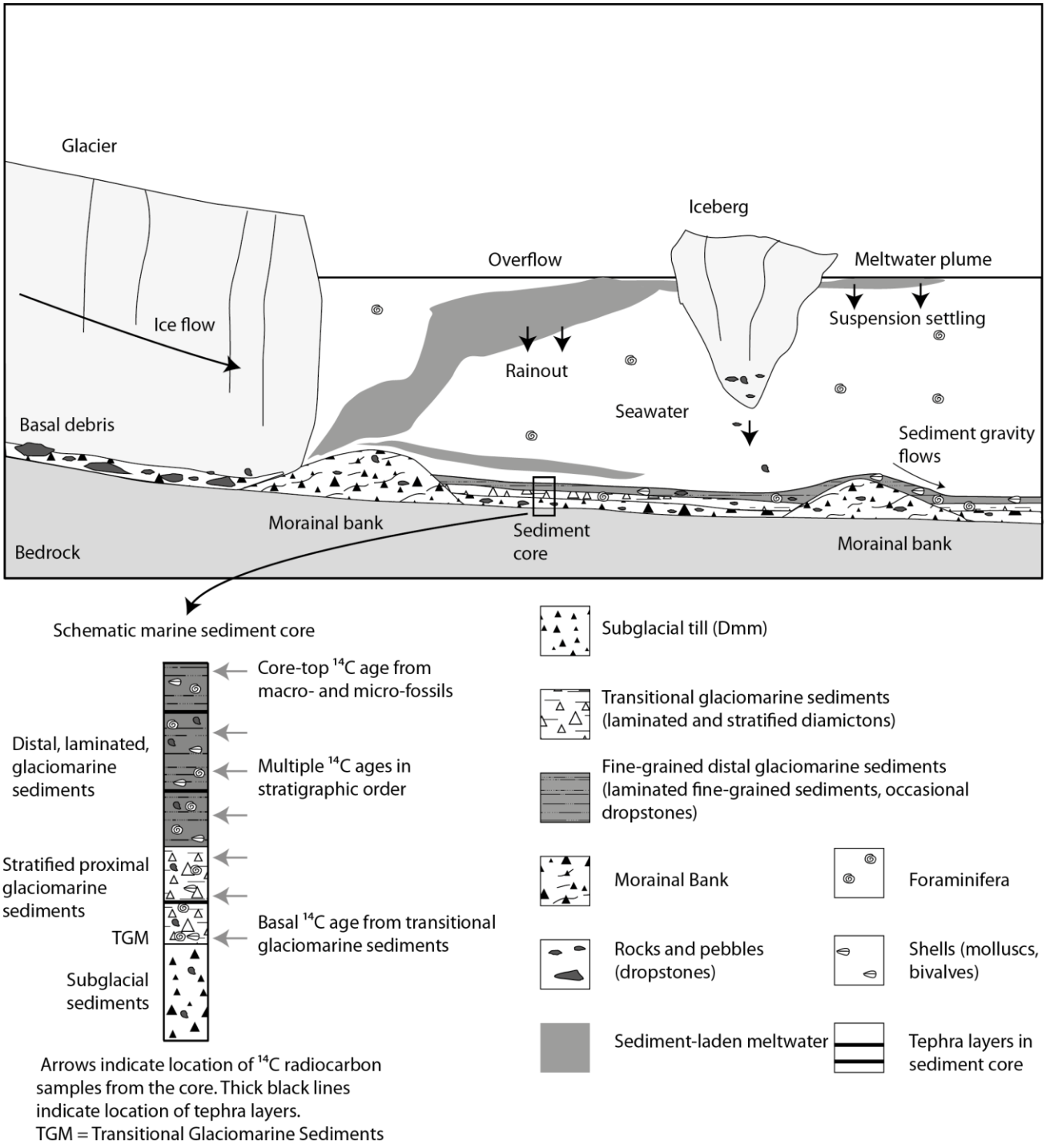

Figure 3. Cartoon illustrating the different facies on glaciated continental shelves such as around Antarctica, and the sampling patterns for radiocarbon dating. This method can be used in conjunction with tephrochronology if visible tephra or cryptotephra layers are present in the sediment core. In this scenario, a retreating ice sheet has deposited morainal banks or grounding zone wedges at locations where the ice margin stabilised. Subglacial diamicton (till) is deposited across the ocean floor, overlain by proximal glaciomarine sediments (transitional glaciomarine sediments) and then distal glaciomarine sediments. Reworked shells within the till can provide minimum bracketing ages for the ice advance, and in situ *shells and microfossils from the transitional glaciomarine sediments provide a maximum bracketing age for the till and a minimum age for the timing of deglaciation.*

Radiocarbon dating of marine materials requires correction for a global marine reservoir effect (MRE), which varies spatially and temporally in response to changes in oceanic and atmospheric circulation and ventilation between the ocean and the atmosphere (Alves et al., 2018; Bondevik et al., 2006; Heaton et al., 2020; Ortlieb et al., 2011). Surface-ocean environments are typically depleted of ^{14}C compared with the atmosphere (Heaton et al., 2020). Because oceanic carbon is not in isotopic equilibrium with the atmospheric carbon reservoir, radiocarbon ages from marine materials provide older apparent ages than terrestrial counterparts. Deep ocean masses with low radiocarbon concentrations may yield ages older by several hundred years. Global marine reservoir values have been estimated for the last 22,000 years at a decadal resolution, with a current MRE value of 400 years (Hughen et al., 2004; Ortlieb et al., 2011). This globally averaged MRE is included in the Marine20 radiocarbon calibration curve (Heaton et al., 2020; Reimer et al., 2013).

However, marine correction varies regionally, especially in high-latitude coastal zones (see Dalton et al., 2020; Hall et al., 2010; Ó Cofaigh et al., 2014). This requires the worldwide quantification of the local parameter Δ*R*, which is the local variation from the global average MRE (Alves et al., 2018). Whilst the MRE changes over time, for any specific location, Δ*R* is assumed to be constant over time (Heaton et al., 2020). Pre-bomb estimates for Δ*R* across a wide range of locations is reported by (Reimer and Reimer, 2001) and a database is maintained online at http://calib.org/marine.

In Antarctica, present-day marine species have radiocarbon 'ages' of ~1200 ± 200 cal. years (Ingólfsson, 2004; Sterken et al., 2012; Verleyen et al., 2011) (i.e. a Δ*R* of 800 ± 200 years taking into account the global MRE of 400 years). In coastal tropical regions, such as the western coast of Chile and Peru, the upwelling of deep ^{14}C-depleted waters to the surface results in high regional reservoir effects. In Chile, the modern *ΔR* value has been calculated as 190 ± 40 years (Stuiver and Braziunas, 1993), but was updated by Ortlieb et al. (2011) to 253 ± 207 years during the Twentieth Century. However, this *ΔR* value fluctuated over the Holocene (Table 1). In many places, radiocarbon sampling of the surficial sediments provides a 'core-top' age that is used to correct stratigraphically down-core ages for the marine reservoir (Figure 3) (Andrews et al., 1999; McKay et al., 2008).

Table 1. Example of ΔR values along the Chile-Peru coastline, from Ortlieb et al., 2011.

Time range	***ΔR* value**
Prior to 10,400 cal. BP	511 ± 278 years
10,400 to 6840 cal. BP	511 ± 278 years
5180 to 1160 cal. BP	226 ± 98 years
1000 cal. BP to present	355 ± 105 years
Early Twentieth Century	253 ± 207 years

2.6 Radiocarbon quality assurance protocols

High-quality radiocarbon ages dating glacial landforms should be taken from known and uncontaminated sample material. For bulk ages, the organic content should be more than 5% when measured on loss-on-ignition (LOI). Bulk samples (including gyttja, organic silt, carbonate clasts) are considered lower quality than individual samples from plant macrofossils. Uncalibrated ages should be presented with full errors to enable recalibration with modern calibration curves. In cores, high-quality ages would have multiple and stratigraphically consistent ages. The $\delta^{13}C$ content should be published. High-quality ages would have appropriate $\delta^{13}C$ values (-25‰ to -32‰ for terrestrial plants; -15‰ for marine plants; -0‰ for marine carbonates) (Lowe and Walker, 2014). High-quality ages would be within the ranges of calibration datasets (Hogg et al., 2013; Reimer et al., 2013). For marine radiocarbon ages, the ΔR should be well understood, justified and provided. Radiocarbon ages should not be derived from freshwater taxa (ostracods, freshwater algaes, aquatic mosses).

3 Cosmogenic nuclide dating

3.1 Introduction to cosmogenic nuclides

Cosmogenic nuclide dating has been widely applied worldwide over the last 20 years (Balco, 2011). It relies on the accumulation of cosmogenic nuclides in materials on the Earth's surface. As cosmic rays have a short attenuation length, and cannot pass through substantial thicknesses of rock, water, ice and sediment, glacially transported rocks and ice-scoured bedrock are shielded from cosmic rays until they are exposed by recession of ice to the atmosphere at the Earth's surface. Upon deposition and recession of the ice, cosmogenic isotopes begin to accumulate in the upper faces of minerals in rocks. These can be measured, and if the production rate is known, the 'exposure age' can be calculated. If the rock is then buried, the divergence between two isotopes with different half-lives (commonly ^{10}Be and ^{26}Al) allows a 'burial age' to be determined.

There are six key isotopes that are useful for cosmogenic nuclide dating in the Earth's surface (^{10}Be, ^{26}Al, ^{3}He, ^{21}Ne, ^{36}Cl, ^{14}C). ^{10}Be is applied most commonly for exposure-age and burial dating of glacial landforms. These isotopes allow exposure or burial age dating over a range of timescales, from hundreds to several million years. In practice, the key limiting factor on using exposure age dating on glacial landforms is the tendency for landforms such as moraines to degrade and rocks to weather away over time, producing scatted ages (Heyman et al., 2011; Ivy-Ochs and Briner, 2014). This means that over longer timescales dating back past the Mid-Pleistocene in exposed locations, exposure-age dating is less applicable than cosmogenic burial dating.

The principals, methods and numerical theories and equations for cosmogenic nuclide dating have been thoroughly reviewed elsewhere (Balco, 2011; Cockburn and Summerfield, 2004; Darvill, 2013; Dunai and Lifton, 2014; Gosse and Phillips, 2001; Granger et al., 2013; Heyman et al., 2016; Ivy-Ochs and Briner, 2014; Ivy-Ochs and Kober, 2007; Jones et al., 2019). The key principles and applications are summarized briefly here, and then sampling methodologies and data analysis protocols are discussed.

3.2 Application in glacial environments

3.2.1 Exposure-age dating

Exposure-age dating is particularly useful for reconstructing deglacial chronologies because temperate, erosive glaciers create fresh rock surfaces, theoretically removing rock with previous exposure to the cosmic ray flux (Balco, 2011). It can be used in the absence of organic matter, and so is applicable even in dry, windy, cold environments like Antarctica, as well as temperate tropical mountain glaciers. It does not suffer from the limitations of methods like lichenometry or dendrochronology, which can have poorly known ecesis times and be susceptible to variations in microclimate. Unlike radiocarbon dating, where there is a lag for the onset of organic matter formation and sedimentation following deglaciation, exposure-age dating provides a direct age for the date of moraine formation or glacial retreat, rather than bracketing ages (Balco, 2011). Well-constructed and empirically validated production rates and scaling schemes mean precision is increasing and the technique widely applicable. It works over a large timescale and is relatively straightforward to apply in the field. A number of inventive methods have been applied to reconstruct deglacial chronologies (Figure 4).

Exposure-age dating is frequently applied to date the timing of the deposition of glacially transported boulders (Applegate et al., 2012; Davies et al., 2019; Hein et al., 2010; Heyman et al., 2011; Mendelová et al., 2020; Putnam et al., 2013). ^{10}Be exposure-age dating of felsic, phaneritic or sandstone glacially transported boulders on glacial moraines is perhaps the most widely applied form of exposure age dating (e.g., Davies et al., 2018; Joy et al., 2014; Kaplan et al., 2020, 2016; Kelly et al., 2008; Reusche et al., 2014; Reynhout et al., 2019; Sagredo et al., 2018). In this scenario, boulders in a stable position on a moraine ridge crest are sampled, and the age is presumed to be equal to the age of moraine formation (Figure 4). This application of the method is particularly useful because moraines represent a decisive period of time when the glacier was in equilibrium with climate, and maintained its position long enough to build the moraine. The timing of moraine formation can be compared to proxy records of palaeoclimate, shedding insights into glacier-climate interactions. Therefore, reconstructing the timing of moraine formation is of particular interest to glacial geologists (Kaplan et al., 2020; Mackintosh et al., 2017; Sagredo et al., 2018).

Other studies have focused on using exposure ages to reconstruct vertical thinning histories, rather than horizontal recession from a moraine (e.g., Boex et al., 2013; Hormes et al., 2013; Johnson et al., 2014, 2012; Lindow et al., 2014; Mackintosh et al., 2007; Stone et al., 2003). Here, samples from either ice-scoured bedrock or glacially transported boulders or cobbles are taken in a vertical transect from a mountain summit downwards. Linear rates of deglaciation can be estimated by calculating the distance and age offset between dated positions (Jones et al., 2019). These data can be used to calculate rates of ice surface lowering (Small et al., 2019).

Exposure age dating can be used to constrain the timing of ice recession from ice-scoured bedrock, and can be paired with dating glacially transported boulders (Corbett et al., 2013, 2011). This can avoid the limitations associated with moraine degradation (Ivy-Ochs and Briner, 2014). However, glacial erosion of less than ~3 m can lead to incomplete removal of nuclides that accumulated during previous exposures. This method is likely to be therefore more appropriate in temperate, deeply eroded alpine valleys (e.g., Guido et al., 2007), with inheritance more likely in high elevation, high latitude regions dominated by cold-based ice (Fabel et al., 2002; Stroeven et al., 2002; Sugden et al., 2005).

In places devoid of sediment, soil, vegetation and organic matter that can obscure the cosmogenic nuclide signal, and where large boulders are few in number, such as nunataks above ice sheets, ^{10}Be exposure ages

can be obtained from smaller glacially abraded quartz-bearing cobbles and pebbles on bedrock (Balco et al., 2013; Bentley et al., 2010; Dong et al., 2016; Hein et al., 2017). Dating erratic cobbles or boulders directly on bedrock can be especially useful if inheritance (nuclides from a previous exposure) is anticipated within the bedrock due to low erosion rates under cold-based ice (Balco, 2011; Bentley et al., 2010; Fabel et al., 2012). Sampling cobbles or boulders resting on bedrock limits clast cycling through the active layer (Hein et al., 2016). If signs of glacial abrasion and transport (erratic lithology, striations, edge-rounded) are clear on the cobbles, this may be taken to indicate negligible erosion. Self-shielding and post-depositional movement is limited in clasts resting on flat bedrock and thinner than ~5 cm (Hein et al., 2016). Care should be taken to ensure that samples could not have reached these positions by colluvial processes after deglaciation (Balco et al., 2013).

For older glaciations where moraine degradation and boulder erosion can make cosmogenic nuclide exposure age dating challenging, cobbles on outwash gravels can also be targeted (Hein et al., 2009). In Patagonia, the arid, windy conditions help ensure continuous surface exposure of surface cobbles. Here, these data revealed a glacial advance during MIS 8, with outwash cobbles yielding exposure ages ~100 ka older than moraine boulders.

Exposure ages can also be used to date the timing of ice-dammed glacial lake drainage (Davies et al., 2018; Fabel et al., 2010; Hein et al., 2010; Thorndycraft et al., 2019) and for dating cobbles within glaciofluvial outwash (Hein et al., 2017, 2011). This is applicable because the cosmic ray flux is strongly attenuated by 2 m of water (Gosse and Phillips, 2001), so boulders deposited below shorelines or perched deltas will constrain the timing of lake-level fall. Figure 4 illustrates some of the ways in which exposure-age dating can be used to understand deglacial chronologies.

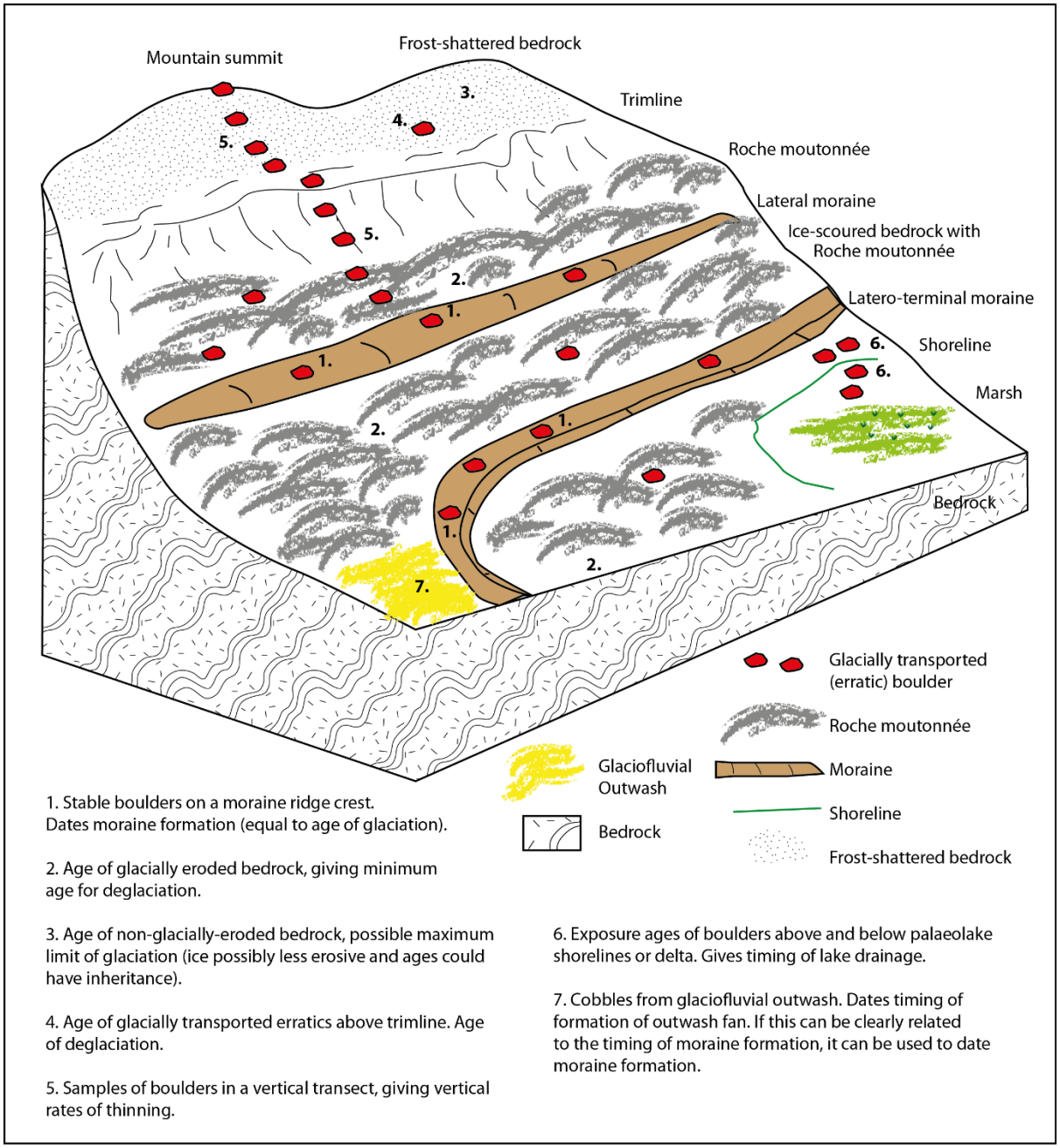

Figure 4. Cartoon illustrating some of the different ways in which exposure-age dating can be used to understand deglacial histories.

3.2.2 Burial dating

Depth profiles use a number of samples (ideally >5) through a sedimentary unit to provide a single surface exposure age based on cosmogenic nuclide concentration at different depths (Darvill, 2013). Sediment burial can be dated by the radioactive decay of cosmogenic nuclide minerals (^{10}Be and ^{26}Al), provided that the sediments were exposed prior to burial (Granger and Muzikar, 2001). This method can be applied over million-year timescales, and can be essential for dating older glacial deposits where moraines are severely degraded (Darvill et al., 2015), or older outwash fans where boulders have weathered away (Ivy-Ochs et al.,

2013). It is straightforward if sediment burial is deep enough to prevent the ongoing formation of cosmogenic nuclides, but more complex if the sediment is insufficiently shielded.

Simple burial dating has been used to date outwash fans and give surface exposure ages in Patagonia. A modelled nuclide attenuation profile through several depth samples will yield a most probable age for surface exposure as well as average inheritance (nuclide concentrations deeper than the penetration of cosmic ray reactions) and surface erosion (projecting measured nuclide concentrations to the modelled surface according to the expected attenuation curve) in the unit (Hein et al., 2009; Hidy et al., 2010; Marrero et al., 2016a). Exposure ages from depth profiles can be strengthened using single exposure ages from cobbles on the unit surface, to provide a check on the modelled exposure age and surface inflation/deflation (Cogez et al., 2018; Darvill et al., 2015; Hein et al., 2017, 2011, 2009). It is also possible to reconstruct more complicated depositional histories using multiple cosmogenic nuclides (Balco and Rovey, 2008; Granger and Muzikar, 2001; Häuselmann et al., 2007; Hein et al., 2009). The depth-profile method may be particularly useful for degraded moraines, fans, or other landforms deposited prior to the last glacial cycle (Cogez et al., 2018; Darvill et al., 2015; Hein et al., 2017, 2010; Ivy-Ochs et al., 2013).

3.3 Principles of cosmogenic nuclide dating

3.3.1 Production of cosmogenic nuclides

The Earth is continuously bombarded from all directions by cosmic radiation (Balco, 2011; Dunai and Lifton, 2014; Gosse and Phillips, 2001). These cosmic rays largely originate from Supernova explosions from the galaxy and beyond our Solar System, and, at the top of our atmosphere, comprise high-energy protons (87%), alpha particles (12%) and heavy nuclei (1%). When these high-energy particles enter our atmosphere, these primary cosmic rays interact with atoms to produce secondary cosmic rays. The high-energy primary cosmic rays are in excess of the binding energies of atomic nuclei. Spallation is a reaction that occurs when nucleons are sputtered off target nuclei following the collision of a primary cosmic ray with a target atom (Dunai and Lifton, 2014). This leaves behind a lighter residual nucleus, such as those shown in Table 2. These spallation-induced nuclei continue in the same direction as the primary cosmic ray, and retain sufficient energy to continue to induce spallation reactions in other target minerals. This results in a nuclear cascade through the Earth's atmosphere, forming meteoric ^{14}C, ^{10}Be, and other cosmogenic nuclides. Energy lost with each interaction means that the mean energy of the secondary neutron flux at sea level is substantially lower than that of the primary flux (Dunai and Lifton, 2014).

The collisions in the upper atmosphere also produce negatively charged muons. They have a greater penetration depth than nucleons, and interact only weakly with matter (Dunai and Lifton, 2014). They are the most abundant cosmic ray particles at sea level. However, spallation reactions with the nucleonic component dominate atmospheric and terrestrial cosmogenic nuclide production (Table 2).

Eventually, the neutrons in the nuclear cascade slow down to energies corresponding to the temperature of their surroundings (Dunai and Lifton, 2014). These "thermal neutrons" can then be captured by nuclei. In some cases (^{3}He, ^{36}Cl), this is an important production source for cosmogenic nuclides.

Terrestrial cosmogenic nuclides are therefore produced in rocks by these interactions between secondary cosmic radiation and minerals at the Earth's surface. The six most commonly used cosmogenic isotopes, which have well-established production rates at the Earth's surface that are large enough to be measured, and long-enough half-lives to be useful, are listed in Table 2.

Table 2. Major cosmogenic nuclides used in geomorphological research, their target elements and minerals, reaction pathways and production rates. Multiple sources (Borchers et al., 2016; Darvill, 2013; Dunai, 2010; Granger et al., 2013; Ivy-Ochs and Kober, 2007; Nishiizumi et al., 2007). Global production rates are given in atoms per gram per year, after Borchers et al. (2016).

Cosmogenic nuclide	Main target elements	Applicable rocks and minerals	Reactions	Half-life	Applicable time range	Production rate (LSD Sa scaling scheme)
^{3}He	Many, including Li	Olivine, pyroxene	Spallation (100%) Thermal neutron capture (on Li via ^{3}H)	Stable	To millions of years	Quartz: 114.55
^{21}Ne	Mg, Al, Si	Quartz, olivine, pyroxene	Spallation (>96.4%)	Stable	Tens of thousands to millions of years	
^{10}Be	O, Si	Quartz (sandstones, granites, gneisses, etc.)	Spallation (96.4%) Muons (3.6%)	1.36 Ma	Ages from hundreds to several million years	Quartz: 3.92
^{26}Al	Si	Quartz (sandstones, granites, gneisses, etc.)	Spallation (95.4%) Muons (4.6%)	0.7 Ma	Ages to several million years	Quartz: 28.54
^{36}Cl	K, Ca, Cl (Fe, Ti)	All rock types. Basalts; volcanic rocks; limestones and carbonate rocks	Thermal neutron capture (from Cl and K) Muons (4.6% from K; 13.4% from Ca)	0.3 Ma	To one million years	Ca: 56.27 K: 156.09
^{14}C	O, Si	Quartz (sandstones, granites, gneisses, etc.)	Spallation (82%) Muons (18%)	5.73 ka	To 20,000 years	Quartz: 12.76

Of these isotopes, ^{10}Be is used most widely to date glacial landforms such as moraines (Granger et al., 2013). This is because its production rate has been well studied and calibrated (Balco et al., 2009; Borchers et al., 2016; Kaplan et al., 2011; Putnam et al., 2010; Small and Fabel, 2015), and because it forms easily from Si and O in quartz, a widespread and common mineral at the Earth's surface. Quartz is resistant to weathering, ubiquitous, and has a simple stoichiometric chemistry (Gosse and Phillips, 2001). For this reason, glacially transported felsic phaneritic rocks (granites) are often targeted for exposure age dating. Granites are resistant to weathering and durable, and can be transported long distances. ^{10}Be also has a long half-life, making it useful for long exposures. ^{10}Be has routinely good precision in AMS measurements, a standardized chemistry procedure (Nishiizumi et al., 2007), and the isotope ^{9}Be is rare in quartz, making it simpler to measure (Granger et al., 2013). It has been used to date glacial landforms from the mid-Pleistocene (e.g.,

Hein et al., 2017, 2009; Mendelová et al., 2020). It has also been applied to date young moraines that date from the last few hundred years in temperate environments (e.g., Kaplan et al., 2016; Schaefer et al., 2009; Schimmelpfennig et al., 2014). Challenges for ^{10}Be dating include that atmospheric ^{10}Be is a significant source of contamination, so quartz grains must be etched and cleaned in the measurement process (Gosse and Phillips, 2001).

^{10}Be can be paired with ^{26}Al, which can highlight inheritance issues (Bentley et al., 2006; Fabel et al., 2002). Both isotopes form in quartz, but have different half-lives. The divergence of the two isotopes can be an indicator for prior exposure. The production rate of ^{26}Al is higher than that of ^{10}Be (Table 2). It can be difficult to measure low ^{26}Al/^{27}Al in quartz with high Al contents (Gosse and Phillips, 2001).

^{14}C can be applied to shorter chronologies (> 30 kyr), especially to Holocene glacial histories (Goehring et al., 2011). The short half-life makes it applicable where erosion rates are low and inheritance may be an issue (Gosse and Phillips, 2001; Miller et al., 2006; White et al., 2011), or exposure histories may be complex (Goehring et al., 2013). It is suitable for quartz-bearing rocks, and can be paired with ^{26}Al and ^{10}Be (Hippe et al., 2014; White et al., 2011), but potential contamination can make sample preparation difficult and expensive (Lifton et al., 2001).

^{36}Cl can be used on a range of lithologies, and is often used on volcanic rocks and basalts that are low in quartz, prohibiting ^{10}Be dating (Briner et al., 2001; Çiner et al., 2015; Sarıkaya et al., 2017; Schimmelpfennig et al., 2009). However, production rates are less well constrained than those for ^{10}Be, because the multiple pathways for production on multiple elements are difficult to decipher (Gosse and Phillips, 2001; Marrero et al., 2016b).

^{3}He has a high production rate and low detection limit in a conventional AMS, so can be used to date younger exposure ages. As it is stable, it can also be used to date longer exposure ages (Goehring et al., 2010). The production rate is better quantified than for ^{21}Ne (Gosse and Phillips, 2001). However, it diffuses rapidly in quartz and fine-grained groundmass in aphanitic rocks, and a correction for radiogenic, nucleogenic and magmatic ^{3}He is necessary. There is also a greater risk of inheritance as it is a stable nuclide. ^{3}He can be used to date lavas without quartz (e.g., Espanon et al., 2014; Johnson et al., 2009). The availability of well-preserved lava flows with independent age control means that production rates are well distributed spatially (Goehring et al., 2010). ^{21}Ne is suitable for dating extremely long exposures, because it is stable (Gosse and Phillips, 2001). This does mean that inheritance may be more of an issue for this isotope. A correction of radiogenic or nucleogenic ^{21}Ne is required.

3.3.2 Production rate

The *production rate* calculates the rate that a particular cosmogenic nuclide is produced at the sampling site. It is expressed in units of atoms produced per year per gram of target material (Borchers et al., 2016). The *in situ* production rate varies according to latitude, altitude, and the thickness and density of a sample (Darvill, 2013; Dunai, 2000; Lal, 1991; Stone, 2000). Production rates are nuclide-specific and can be established regionally using independently dated features such as radiocarbon-dated moraines (Balco et al., 2009; Kaplan et al., 2011; Putnam et al., 2010), varved records with tephra (Small and Fabel, 2015), argon-dated volcanic lavas (Foeken et al., 2012), or tree-ring chronologies (Kubik et al., 1998). Published production rates are normalized to sea-level and high-latitude (SLHL), and then must be scaled using a *scaling scheme* according to altitude and latitude (Borchers et al., 2016). Global production rates are provided by Borchers et al. (2016) (Table 2). Generally, production rates should be applied locally and compared with global

production rates. Production rates for ^{10}Be are best quantified. Some examples of local production rates are shown in Table 3.

ICE-D (Informal Cosmogenic-nuclide Exposure-age Database; http://ice-d.org) is a production rate database that includes published empirical calibration rate studies (Balco, 2020; Martin et al., 2017). This allows the user to select a global, regionally averaged or local production rate for age calculation. It is compatible with several cosmogenic nuclide calculators, including CRONUS-calc.

Table 3. Examples of regional production rates for ^{10}Be, scaled to SLHL. For a complete database, the reader is referred to ICE-D.

Location	Reference	^{10}Be production rate (atoms/g/yr)	Comments and scaling scheme	Calibration method
Global	Borchers et al. (2016)	3.92	LSDn (Sa) scaling scheme	Analysis of global datasets
Patagonia	Kaplan et al. (2011)	3.71 ± 0.11	When using a time-dependent scaling method that incorporates a high resolution geomagnetic model.	Independently dated moraines (^{14}C)
Southern Alps, New Zealand	Putnam et al. (2010)	3.74 ± 0.08	Using 'Lm' scaling scheme. Relative to '07KNSTD'	Independently dated moraines (^{14}C)
Scotland	Small and Fabel (2015)	4.26 ± 0.21	Using 'Lm' scaling scheme	Glacial lake shorelines independently dated with varves and tephra
North America	Balco et al. (2009)	4.26 ± 0.21	Using 'Lm' scaling scheme	Independently dated Late Glacial landforms
Scandinavia	Stroeven et al. (2015)	4.13 ± 0.11	Using 'Lm' scaling scheme	Varved lake sediments
Scandinavia	Stroeven et al. (2015)	3.95 ± 0.10	Using 'LSDn' scaling scheme	Varved lake sediments

3.3.3 Scaling scheme

The primary cosmic rays approaching Earth are affected by the Earth's magnetic field and solar activity (Darvill, 2013), with most rays penetrating the atmosphere at the poles and least at the equator. The ability of a ray to penetrate the atmosphere is determined by the angle of incidence and their location relative to geomagnetic field lines. Variations in the Earth's magnetic field cause variations in the long-term primary ray production, and affect the flux of cosmic radiation at the Earth's surface. The regional or global production rate must therefore be scaled for latitude and altitude to create an estimate of the site-specific production rate. These scaling schemes take into account altitude and latitude (Dunai, 2001; Stone, 2000), variations in

geomagnetic field strength, changes in solar activity (Lifton et al., 2008), and temporal changes in the energy spectrum (Lifton et al., 2014).

There are six primary scaling schemes commonly used (Table 4). At latitudes greater than 30° and elevations below 3000 m, there is little difference between the scaling schemes (Dunai and Lifton, 2014). However, differences of up to 30% may arise between models at lower latitudes and higher elevations. Users should ensure consistency when comparing ages between different studies that may have used different production rates and scaling factors (Balco, 2011; Darvill, 2013).

Neutron-monitor based models (De, Du) are prone to overestimate the altitude dependence of cosmogenic-nuclide production (Martin et al., 2017). The LSDn scaling scheme (Lifton-Sato-Dunai) is a newer, more complex scaling scheme based on particle transport models (Lifton et al., 2014), and is recommended by Borchers et al. (2016). It provides information available neither from the traditional Lal (St) scaling scheme, or the neutron-monitor based scaling schemes (Du, Li, De) (Marrero et al., 2016a). LSDn also provides a separate scaling factor for each nuclide, rather than a single scaling factor for all nuclides (*ibid*). LSDn has a good agreement with the older Lal-Stone model (Martin et al., 2017).

The production rate therefore changes, or is scaled, through time, according to the scaling scheme used and the sample's latitude, longitude and elevation (Balco et al., 2008). Time-independent scaling schemes (St) result in a constant production rate.

Table 4. Scaling schemes for cosmogenic nuclide production. Numerous sources (Balco et al., 2008; Dunai and Lifton, 2014; Marrero et al., 2016a).

Scaling scheme abbreviation	**References**	**Time dependency (constant or variable production rate)**	**Description**
St (Lal/Stone)	Lal (1991); Stone (2000)	Time-independent (constant production rate)	Altitude, latitude taken into account. Does not take into account magnetic field variations.
Lm ('Lal modified')	Lal (1991); Nishiizumi et al., (1989); Stone (2000)	Time-dependent (variable production rate)	Time-dependent version of St, based on time-variation in the dipole magnetic field intensity. Production rates vary with time according to magnetic field changes.
De (Desilets)	Desilets et al. (2006)	Time-dependent	Based on neutron monitor measurements and incorporating dipole and non-dipole magnetic field measurements. Production rates vary with time according to magnetic field changes.
Du (Dunai)	Dunai (2001)	Time-dependent	Based on neutron monitor measurements and incorporating dipole and non-dipole magnetic field measurements. Production rates vary

			with time according to magnetic field changes.
Li (Lifton)	Lifton et al. (2005)	Time-dependent	Based on neutron monitor assessments and incorporates dipole and non-dipole magnetic field fluctuations and solar modulation. Production rates vary with time according to magnetic field changes and changes in solar output.
LSDn (Sf, Sa) (Lifton-Sato-Dunai)	Lifton et al. (2014)	Time-dependent	Based on equations from nuclear physics model. Incorporates dipole and non-dipole magnetic field fluctuations and solar modulation.

3.3.4 Attenuation length

The high-energy component of cosmic radiation follows an exponential decrease as a function of the cumulative mass penetrated perpendicular to the surface of the rock (Gosse and Phillips, 2001). The *attenuation length* (Λ) is the thickness of a slab of material (rock, air, water, sediment, snow) required to attenuate the intensity of the cosmic-ray flux by a factor of e^{-1}, due to scattering and absorption processes. The attenuation length varies with altitude and latitude, because the geomagnetic field and atmosphere change the energy spectrum (Gosse and Phillips, 2001). The attenuation coefficient is expressed in terms of units of mass length (g cm^{-2}) because the length depends on the total mass traversed and is therefore a function of the material's density. The attenuation length of solid rock, with a typical bulk density of 2.7 g cm^{-3}, is 121 – 170 g cm^{-2}, and the thickness of rock required to attenuate the cosmic ray flux by a factor of e^{-1}, is 45 to >65 cm. In practice, the attenuation length (Λ) is usually taken to be a constant, at 160 g cm^{-2} (Balco, 2011; Balco et al., 2008; Gosse and Phillips, 2001). Length in units of cm can be determined if densities are known and constant (Table 5), by dividing the attenuation length of 160 g cm^{-2} by the material density.

Table 5. Lengths in cm for various materials required to attenuate the cosmic ray flux.

Material (bulk density (ρ))	**Thickness of material required to attenuate intensity flux by a factor of e^{-1}, where Λ = 160 g cm^{-2} (assumes a constant density)**
Granite (2.7 g cm^{-3})	59.3 cm
Granite (2.6 g cm^{-3})	61.5 cm
Basalt (2.5 g cm^{-3})	64.0 cm
Soil or tuff (2 g cm^{-3})	80 cm
Water (1 g cm^{-3})	160 cm

Ice (0.9167 g cm^{-3})	174.5 cm
Snow (0.25 g cm^{-3})	640 cm

When calculating an exposure age, the sample thickness is therefore a crucial parameter because production by spallation within the rock is assumed to have an exponential depth-dependence with a single attenuation length (160 g cm^{-2}) (Balco et al., 2008). In granite, the spallogenic production rate falls by a factor of two with every ~40 cm of depth, and becomes negligible 2 to 3 m below the surface (Balco, 2011).

3.3.5 Topographic shielding

Exposure-age samples will be shielded by any nearby topography (Balco, 2014; Balco et al., 2008; Codilean, 2006; Darvill, 2013; Gosse and Phillips, 2001; Nishiizumi et al., 1989). Exposure age samples must therefore be corrected with a non-dimensional *shielding factor* (0 to 1). Samples with a shielding factor of 1.0 have no topographic shielding. The shielding factor used in cosmogenic calculators such as CRONUS-Calc is derived from measurements of the elevation to the skyline and the dip and dip direction of the rock surface sampled. This is discussed in more detail under "Sampling Methodologies". The horizon will impede the cosmogenic ray flux, if the obstructions are more than several effective attenuation lengths for spallogenic production (i.e., several metres thick) (Balco et al., 2008). The effect of common topographic shielding is relatively minor; a flat surface at the bottom of a pit with 45° sloping walls would still receive 80% of incoming radiation (Gosse and Phillips, 2001). Horizon shielding of less than 5° is of negligible importance. Shielding will be accentuated if the sampled surface is sloped towards a major topographic obstruction, such as a valley side. This is because, as most incoming radiation is close to vertical, a significant slope on the surface will reduce the radiation flux (*ibid*). The rock surface above the sample will also act to obstruct radiation. Attenuation lengths will be shortened on dipping surfaces, because particles will entre at oblique angles.

Winter snow, water, sand, peat or soil can also act to shield rock surfaces (Gosse and Phillips, 2001). The attenuation lengths for these common materials are given in Table 5. In general, if thicknesses of these relatively low-density materials is small, then shielding is limited. Snow survey data can be used to estimate average snow depth and snow water content, and these data can be used to correct for shielding (Gosse and Phillips, 2001). However, snow cover can be an important and is often a neglected uncertainty in exposure-age calculations (Delunel et al., 2014; Schildgen et al., 2005). Jones et al. (2019) account for snow cover and cover by other materials in the IceTEA calculator.

3.3.6 AMS Standards

^{10}Be and ^{26}Al measurements are made by comparison with a reference standard with a defined isotope ratio (Balco et al., 2008). ^{10}Be concentrations are derived by adding a known quantity of ^{9}Be to a measured weight of quartz, dissolving the quartz, extracting Be, and measuring the ^{10}Be/^{9}Be ratio in an AMS. The AMS therefore compares the isotope ratio to a Be reference material where the isotope ratio has been measured independently (Balco, 2011). The accuracy of the ^{10}Be concentration measurement depends on the accuracy of the absolute isotope ratio assumed in the Standard Reference Material (SRM) (Balco et al., 2008), and knowledge of the ^{10}Be half-life (Balco, 2011). Intercalibration of AMS standards allows the results from

different laboratories to be compared (Fink and Smith, 2007; Kubik and Christl, 2010). Standards are largely resolved for ^{10}Be, ^{26}Al and ^{14}C, but are less well defined for other nuclides (Granger et al., 2013). Prior to Nishiizumi et al. (2007), the assumed half-life of ^{10}Be was 1.5 Ma (e.g. Fink and Smith, 2007). The revision of the half-life by Nishiizumi et al. (2007) to 1.36 ± 0.07 x10^{6} years also revised the value of the NIST ^{10}Be standard (SRM4325) to 2.79 ± 0.03 x10^{-11} ^{10}Be/^{9}Be. This resulted in the 07KNSTD standard, against which all other measurements are currently normalized to.

In cosmogenic nuclide calculators, the standards must be inputted, and nuclide measurements normalized to a reference standard that is compatible with the reference standard used in calibration measurements (Nishiizumi, 2004; Nishiizumi et al., 2007). Common ^{10}Be AMS standardisations are listed in the documentation for the online calculators formerly known as the CRONUS-Earth Online Calculators (https://hess.ess.washington.edu/) and are summarized in Table 6. Authors should always clearly present their standards when giving ^{10}Be results (Balco, 2011; Dunai and Stuart, 2009; Frankel et al., 2010).

Table 6. ^{10}Be standardisations. Sources include Balco et al. (2008), Nishiizumi et al. (2007), Kubik and Chistl (2010) and documentation from CRONUS-Earth (https://hess.ess.washington.edu/math/docs/al_be_v22/standard_names.html and https://hess.ess.washington.edu/math/docs/al_be_v22/AlBe_standardization_table.pdf; both accessed 01.04.2020). Conversion Factor is the factor by which a standardisation is multiplied to make it consistent with the 07KNSTD standardisation. The normalisation is carried out by the CRONUS-Calc ^{10}Be calculator. AMS standards should always be presented when giving ^{10}Be AMS results.

Code	Description	Conversion factor
07KNSTD	After Nishiizumi et al. (2007). Measurements made at PRIME Lab after Nov. 14 2007 were referenced to this standardization. This is the standardization to which internal constants and production rates are based on for the CRONUS-Earth calculator, and all other standardisations will be internally converted to be consistent with 07KNSTD. NIST ^{10}Be standard (SRM4325) is 2.79 ± 0.03 x10^{-11} ^{10}Be/^{9}Be.	1.000
KNSTD	Same standard material as 07KNSTD but with a different nominal isotope ratio that was assumed before the 2007 version. Used by PRIME Lab between 2005 and 2007.	0.9042
NIST_Certified	Produced by National Institute of Standards and Technology (NIST), referred to as SRM4325. Measurements made at PRIME before 2005 used this. Nominal isotope ratio of 2.68 x 10^{-11}	1.0425
NIST_30000	The NIST SRM4325 standard material with assumed isotope ratio of 3.0 x 10^{-11}	0.9313
NIST_30200	The NIST SRM4325 standard material with an assumed isotope ratio of 3.02 x 10^{-11}	0.9251

NIST_30300	The NIST SRM4325 standard material with an assumed isotope ratio of 3.03×10^{-11}	0.9251
NIST_30600	The NIST SRM4325 standard material with an assumed isotope ratio of 3.06×10^{-11}	0.9130
NIST_27900	The NIST SRM4325 standard material with an assumed isotope ratio of 2.79×10^{-11} (equivalent to 07KNSTD)	1.000
BEST433	ETH-Zurich standard material "BEST433" used prior to April 1, 2010. Assumed isotope ratio of 93.1×10^{-12}. After Kubik and Christl (2010)	0.9124
S555	ETH-Zurich standard material "S555" used prior to April 1, 2010. Assumed isotope ratio of 95.5×10^{-12}. After Kubik and Christl (2010)	0.9124
S2007	ETH-Zurich standard material "S2007" used prior to April 1, 2010. Assumed isotope ratio of 30.8×10^{-12}. After Kubik and Christl (2010)	0.9124
BEST433N	ETH-Zurich standard material "BEST433" with revised assumed isotope ratio of 83.3×10^{-12}. After Kubik and Christl (2010). Equivalent to 07KNSTD. Used at ETH in April 2010.	1.000
S555N	ETH-Zurich standard material "S555" with revised assumed isotope ratio of 87.1×10^{-12}. After Kubik and Christl (2010). Equivalent to 07KNSTD. Used at ETH in April 2010.	1.000
S2007N	ETH-Zurich standard material "S2007" with revised assumed isotope ratio of 28.1×10^{-12}. After Kubik and Christl (2010). Equivalent to 07KNSTD. Used at ETH in April 2010.	1.000
STD11	ASTER standard with assumed isotope ratio of 1.191×10^{-11}. Equivalent to 07KNSTD and NIST_27900.	1.000

3.3.7 Erosion Rates

Exposed surfaces will denude over time due to weathering and *in situ* breakdown of rock. The concentration of surface cosmogenic nuclides is sensitive to surface erosion (Gosse and Phillips, 2001). Assuming that rock erosion rates are constant over time, cosmogenic nuclide data can be used to determine an erosion rate, because the concentration of ^{10}Be at the surface of a steadily eroding outcrop surface is inversely proportional to the outcrop's erosion rate (Balco et al., 2008; Gillespie and Bierman, 1995; Portenga et al., 2013). Erosion rates calculated in this way are limited to rock outcrops and boulders. A detailed discussion of erosion rates is beyond the scope of this chapter. Here, this section focuses on the importance and significance of erosion rates for the production of surface exposure ages.

Calculators require an *erosion rate* (cm yr^{-1} or mm kyr^{-1}) to account for the impact of this on the surface exposure age (Granger et al., 2013). Typically low erosion rates of 0.5 to 2.5 mm kyr^{-1} for resistant lithologies in temperate regions will have little impact on samples younger than ~30 kyr (Balco, 2011; Davies et al., 2020; Gosse and Phillips, 2001). Erosion rates are increasingly important for older deposits, even with low erosion rates of 1 mm kyr^{-1} (Hein et al., 2009). However, measured erosion rates are sparse in many regions, and may be spatially and temporally variable, as well as variable according to lithology sampled. Practitioners presenting surface exposure ages should therefore present data with a zero erosion rate, providing a minimum age for the deposit, and one under a clearly reported constant, estimated rate of erosion that is appropriate for the regional climate and lithology (Darvill, 2013).

Typical erosion rates were reviewed by Portenga and Bierman (2011), who compiled and normalized published ^{10}Be erosion rate data (n = 1599). They found that outcrops had a mean erosion rate of 12 ± 1.3 mm kyr^{-1}, median 5.4 mm kyr^{-1}, lower than the mean drainage basin erosion rate of 218 mm kyr^{-1}. These rates varied according to climate zone, rock type and tectonic setting. Erosion rates on sedimentary outcrops are typically 20 ± 2.0 mm kyr^{-1}, metamorphic outcrops have a mean erosion rate of 11 ± 1.4 mm kyr^{-1}, and igneous outcrops have a mean erosion rate of 8.7 ± 1.0 mm kyr^{-1}. Erosion rates of outcrops in polar climates have a mean of 3.9 ± 0.39 mm kyr^{-1}, whilst temperate climates have a mean of 25 ± 2.5 mm kyr^{-1} (Portenga and Bierman, 2011). Measurements on homogenous crystalline rocks have typically yielded low erosion rates of 0.2 mm kyr^{-1}, with 1 mm kyr^{-1} for biotite-rich crystalline rocks, and 5 mm kyr^{-1} for carbonate sedimentary rocks (André, 2002). Estimates of erosion rates on granite in temperate Patagonia include 1.4 mm kyr^{-1} (Kaplan et al., 2005), 0.049 ± 0.02 to 1.31 mm kyr^{-1} (Bourgois et al., 2016) and 0.2 mm kyr^{-1} (Douglass, 2007). Bedrock outcrop erosion rates from the central Appalachian Mountains produced mean ridgeline erosion rates of 9 mm kyr^{-1} (Portenga et al., 2013). Sandstone erosion rates in Antarctica are mostly < 1 mm kyr^{-1} (Hein et al., 2016).

3.3.8 Geological scatter in cosmogenic nuclide dating

Geological scatter is a common issue in exposure-age dating. Moraine exposure ages from a single landform may produce ages that differ by more than the measurement uncertainty (Balco, 2011). The main causes of this in colder environments such as Antarctica is inheritance (Figure 6). Here, clasts may be recycled and undergo repeated periods of exposure, resulting in an inherited signal (Bentley et al., 2010). Bedrock and erratic clasts may be (repeatedly) passively overridden by cold-based, non-erosive ice (Bentley et al., 2006). These incidences, with repeated exposure and shielding, result in a complex exposure history and anomalously old, scattered ages. As a result, Antarctic studies often use the youngest apparent exposure age from a landform as the most reliable in cases of geological scatter (Bentley et al., 2006; Hein et al., 2016).

Co-isotope analysis using ^{26}Al and ^{10}Be, which have different half-lives (Table 2), can also be used to screen for inheritance (Balco, 2011; Bentley et al., 2006; Corbett et al., 2013). The two isotopes will decay at different rates during periods of burial; the ^{26}Al/^{10}Be ratio will therefore evolve from the production ratio of ~6.75. Plotting the ^{26}Al/^{10}Be ratio against ^{10}Be concentration (Figure 5) can illuminate complex inheritance, erosion and burial. In Figure 5, the burial pathways (grey arrows) show how in samples that are buried following initial exposure, it moves left (as ^{10}Be nuclides decay) and downwards (because ^{26}Al decays faster with a shorter half-life) on the co-isotope plot (Corbett et al., 2013). Samples plot in the Burial Zone (light grey shading) if have had one episode of exposure followed by burial (a complex exposure history). Samples for exposure age dating should, ideally, when uncertainties are taken into account, plot within the 'erosion island' (dark grey on Figure 5). They plot here if they have experienced constant (simple) exposure with

erosion. The erosion paths taken according to different erosion rates are highlighted by the finely dashed lines. Samples plot along the constant exposure pathway if they have experienced constant exposure with no erosion. Screening with co-isotope plots such as this can help identify samples for exclusion, but it will only identify samples that have been buried for several tens of thousands of years (Bentley et al., 2006).

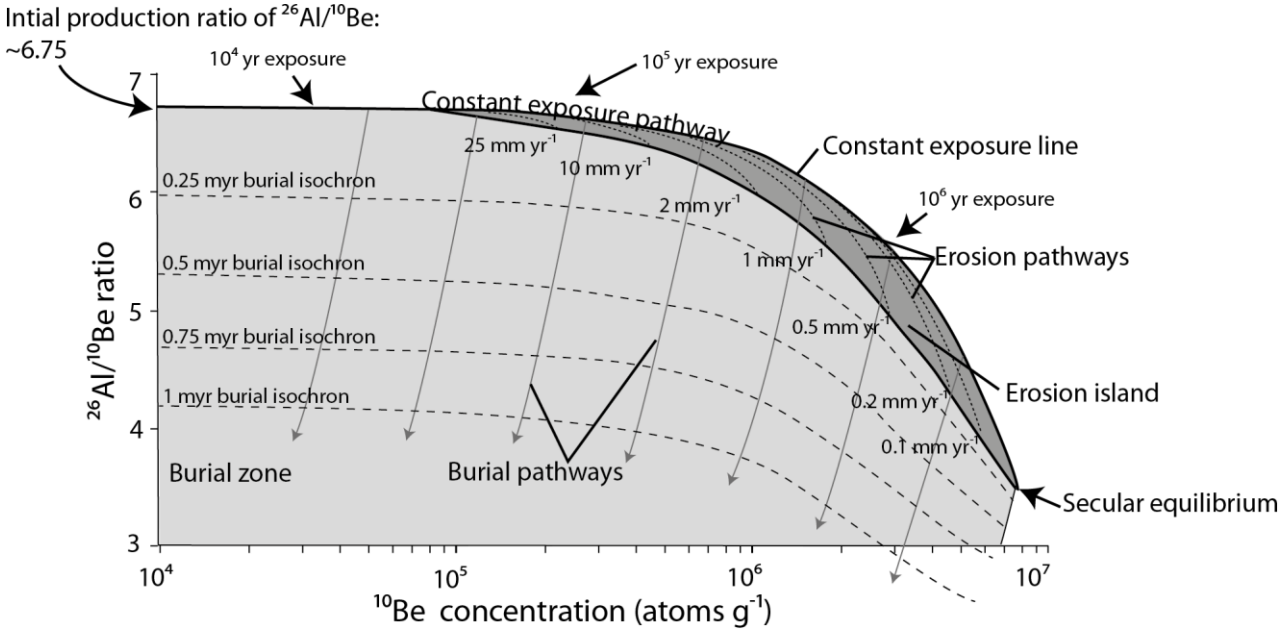

Figure 5. Schematic showing two-isotope cosmogenic data. Modified from Corbett et al. (2013). Pathways for different erosion rates are given in mm yr^{-1}.

Moraines with glacially transported and abraded erratic boulders make good targets for exposure-age dating (Granger et al. 2011), marking a decisive point in the glacier's history. In the ideal case, boulders with no prior exposure history are plucked, abraded and transported by the glacier, and deposited on a moraine in a stable position (Figure 6A) (Heyman et al., 2011). In temperate environments, glacial processes are likely to be more erosive and inheritance less problematic. However, post-depositional processes can result in scatter. This includes rock surface erosion, movement or rolling of boulders as the moraine degrades, exhumation of boulders from within the moraine as the moraine degrades and surface cover is eroded, or soil creep (Applegate et al., 2012; Balco, 2011; Putkonen and Swanson, 2003). The destruction of boulders originally exposed through weathering and the exhumation of younger boulders through surface lowering is a significant challenge when dating moraines that predate the last glacial cycle (Chevalier et al., 2011). This incomplete exposure due to post-depositional shielding followed by moraine degradation causes an underestimation of moraine age, with anomalously young exposure ages and geological scatter (Figure 6C) (Heyman et al., 2011).

Large boulders in stable positions on moraines are least likely to have undergone movement or exhumation in this way, and so make better targets for surface exposure age dating (Granger et al., 2013; Heyman et al., 2016). Exposure ages from larger boulders have a larger fraction of well-clustered exposure ages (Heyman et al., 2016). Short boulders tend to produce younger exposure ages than taller boulders from the same group, with incomplete exposure likely dominating. Shorter, smaller boulders on moraines are more likely to have undergone shielding followed by exhumation during moraine degradation (Heyman et al., 2016).

Single exposure ages from a landform are considered less reliable, and practitioners should seek multiple replicate samples per moraine. For moraines dating from the last glacial maximum or younger, 3 to 5 boulder samples are appropriate, with more boulders required for older, larger moraines (Putkonen and Swanson, 2003). Ideally, cosmogenic nuclide exposure age datasets should include multiple boulders dating a sequence of moraines, which will allow easier identification of outliers. Strategies for dealing with outliers in this case range from excluding anomalously old ages to applying a range of statistical treatments (Applegate et al., 2012; Jones et al., 2019).

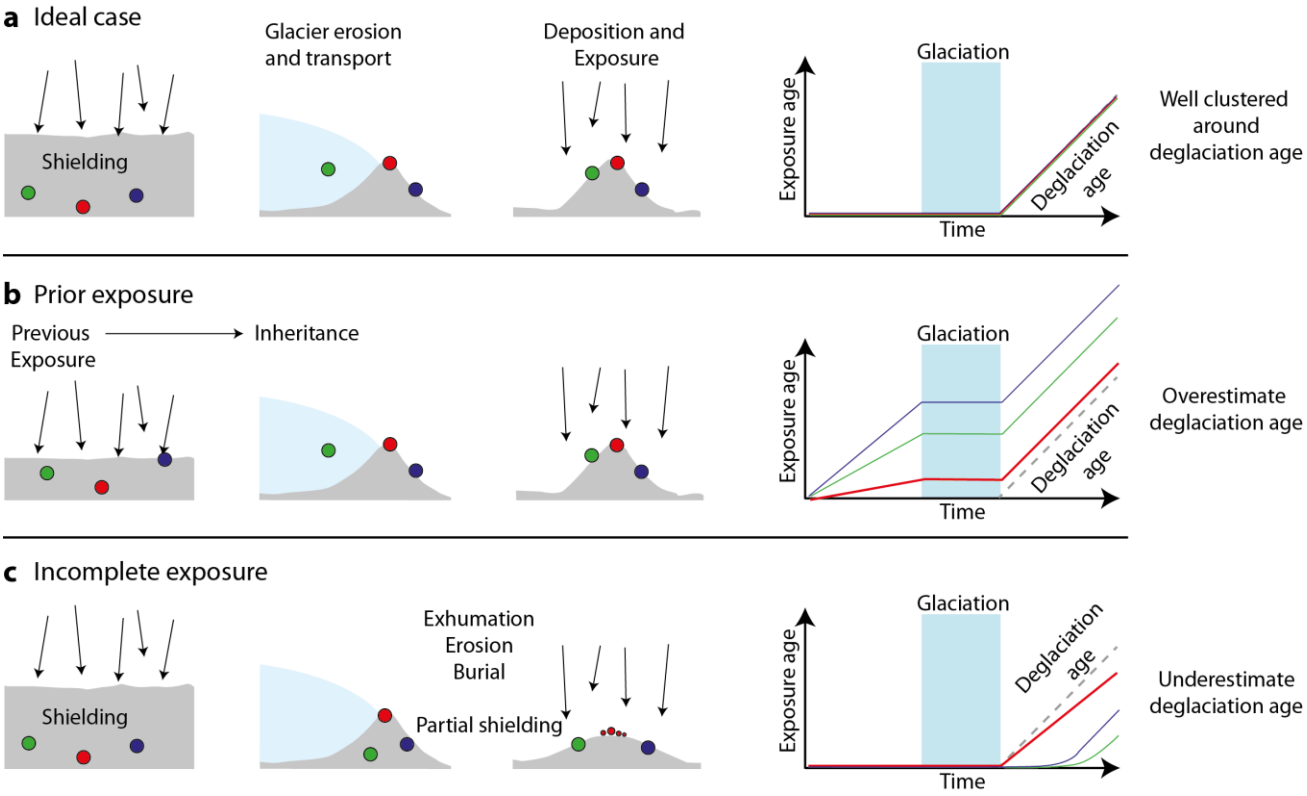

Figure 6. Principles of prior exposure and incomplete exposure and resulting apparent exposure ages. A: the ideal case. The sample has been completely shielded from cosmic rays prior to glaciation, and then continuously exposed since deglaciation. B: the sample is exposed to cosmic rays prior to glaciation and experiences no post-glacial shielding (prior exposure). The apparent exposure age exceeds the deglaciation age. C: If a sample is incompletely shielded from cosmic rays prior to glaciation and partially shielded following deglaciation (incomplete exposure), the apparent exposure age will be younger than the deglaciation age. Adapted from Earth and Planetary Science Letters *302, Heyman et al., "Too young or too old: evaluating cosmogenic exposure dating based on analysis of compiled boulder ages", pages 71-80, Copyright 2011, with permission from Elsevier.*

3.4 Sampling methodologies in glacial environments

3.4.1 Exposure-age sampling methodologies

Sampling strategies for exposure-age dating will depend upon the research objectives, the rock type and target minerals available and resultant choice of isotope, and the local environment. Researchers should in

all cases aim to collect multiple replicate samples where possible, especially in the case where a particular landform (such as a moraine) is to be dated. A fundamental knowledge of the principles of the six cosmogenic nuclides is required in order to design such a sampling strategy. Fundamentally, the sample should contain sufficient target mineral to obtain measurable quantities of the required nuclide.

Careful geomorphological mapping is critical to understand the depositional processes affecting boulders and any post-depositional modification (e.g. Kelley et al., 2014; Koffman et al., 2017; Schaefer et al., 2009). For example, it is important to understand the relationship between moraines, boulders, slope processes and any ice-dammed palaeolakes, as boulders deposited below lake water will have an exposure age that records the timing of lake-level fall, rather than deglaciation (Davies et al., 2020, 2018; Hein et al., 2010; Thorndycraft et al., 2019).

Boulders should only be sampled if the operator can be sure that they were glacially transported, and not deposited by rockfall or other geomorphic processes. Both bedrock and glacially transported boulders should show signs of glacial transport, abrasion, and erosion (faceting, striations, polish, edge-rounding, of a erratic lithology), so that any inherited nuclides have ideally been removed. Multiple boulders should be sampled per moraine, as geological scatter is a common issue in exposure-age dating. This is because moraines degrade over time, and boulders can be weathered away, exhumed, buried, or destroyed by erosion. They may have an inheritance, with cosmogenic isotopes dating from a prior exposure. This can lead to geological scatter (Applegate et al., 2012; Heyman et al., 2016, 2011). Sampling 3 to 5 boulders for moraines dating to the Last Glacial Maximum or younger can help with identification of outliers (Putkonen and Swanson, 2003). Larger boulders more than 0.5 m above the ground height should be targeted in order to minimize the risk of exhumation and post-depositional processes causing geological scatter (cf. Heyman et al., 2016). Boulders should only be sampled where they are in a stable position in the landscape or on the moraine and there is no possibility that they have rolled, rotated, or otherwise moved significantly since deposition (Figure 7). For moraines, ideally boulders should be situated on the moraine crest (e.g. Figure 8).

Cobbles may be sampled where they lie on flat bedrock, and the possibility of cycling through the active layer as a result of periglacial processes can be excluded. Cobbles should be marked with the uppermost surface marked. If they are less than ca 5 cm thick, then attenuation through the sample and self-shielding can be effectively disregarded. Cobbles should however be large enough that they are not moved due to strong winds. They should be sampled from exposed locations where snow cover is likely to be thin or inconsequential. Cobbles should weigh ca 1 kg minimum, so as to increase the likelihood of the required nuclide. They should show signs of glacial transport (abrasion, striations, faceting) and ideally be of an erratic lithology, so that local production of the cobbles can be excluded.

The ideal boulder, rock, landform surface or bedrock surface for sampling should be sufficiently extensive, flat, and horizontal. The angle of the surface will affect the shielding and so should be recorded. Samples should be collected at least 50 cm away from any edges (Gosse and Phillips, 2001). Samples with less topographic shielding are preferable, to avoid the need for additional corrections. Flat surfaces also require fewer corrections for shielding, and so have a greater precision and accuracy. Edges are susceptible to 'edge effects', particularly for nuclides such as ^{36}Cl that are produced by muon capture, as cosmic rays could penetrate from multiple directions. Samples should ideally be taken from the flattest, central, uppermost surface of the boulder, but this can in reality be challenging unless a rock saw or small explosive charge is used. Shielding from snow cover and vegetation can be minimized by choosing boulders that are large and upstanding and above the local topography (e.g. Figure 8A, B, F), as they are more likely to be windswept (Gosse and Phillips, 2001).

A thorough sample description is required in order to calculate shielding and production rate scaling. A hypothetical proforma to assist with this is presented in Figure 7, which follows best-practice guidelines (Darvill, 2013; Gosse and Phillips, 2001). Samples should be sketched, photographed from all angles, and details of location (decimal degrees), elevation (m asl) and geomorphic context should be very carefully recorded. In order to calculate the shielding, the dip and dip direction of the surface and the angle of elevation to the skyline should be recorded at regular intervals. This can be checked with a digital elevation model (DEM) in a geographic information system (GIS) if the horizon is not always visible (Codilean, 2006). The boulder's characteristics should be carefully described, including dimensions and height above ground surface, signs and measurements of weathering or erosion (upstanding quartz veins, weathering pits, flaking), lithology, grain size and quartz content. Sample thickness should be recorded as well.

Samples should be collected with the aim of leaving as little permanent scarring as possible on the landscape. Sampling with a hammer and rock chisel or small charge can be best, as these methods take small flakes and leave little permanent visual impact. Sampling with a rock saw can be easier and quicker, and allows the operator to choose more precisely where to sample, but if this method is used, some time should be spent afterwards to obscure and roughen the straight cuts. Samples should only be taken with the permission of the landowner, and permits may be required in some localities. Ideally, samples should be stored in a durable cloth bag, clearly marked with permanent marker pen.

The volume of sample required depends on the proportion of the target mineral, grain size of the target mineral, and required isotope. Around 1 mg of $^{10}Be/^{9}Be$ is required for AMS analysis. For ^{10}Be dating of quartz-rich rocks (such as a typical granite, with 10% quartz), a minimum of 500 g but ideally around 1 kg of sample should be obtained. Samples from rocks with a younger exposure age should be larger, to obtain the required level of precision (Gosse and Phillips, 2001). In sample processing, material could be lost due to accidental chemistry, and offcuts may be required for thin section or duplicate chemistry. Larger samples will be needed in rocks with a lower quartz content. 5 kg of rock could be required, for example, for the analysis of fine-grained quartz-poor rocks (*ibid*). Whole-rock analyses of ^{36}Cl do not require mineral separates, and so smaller samples of 500 g may be appropriate.

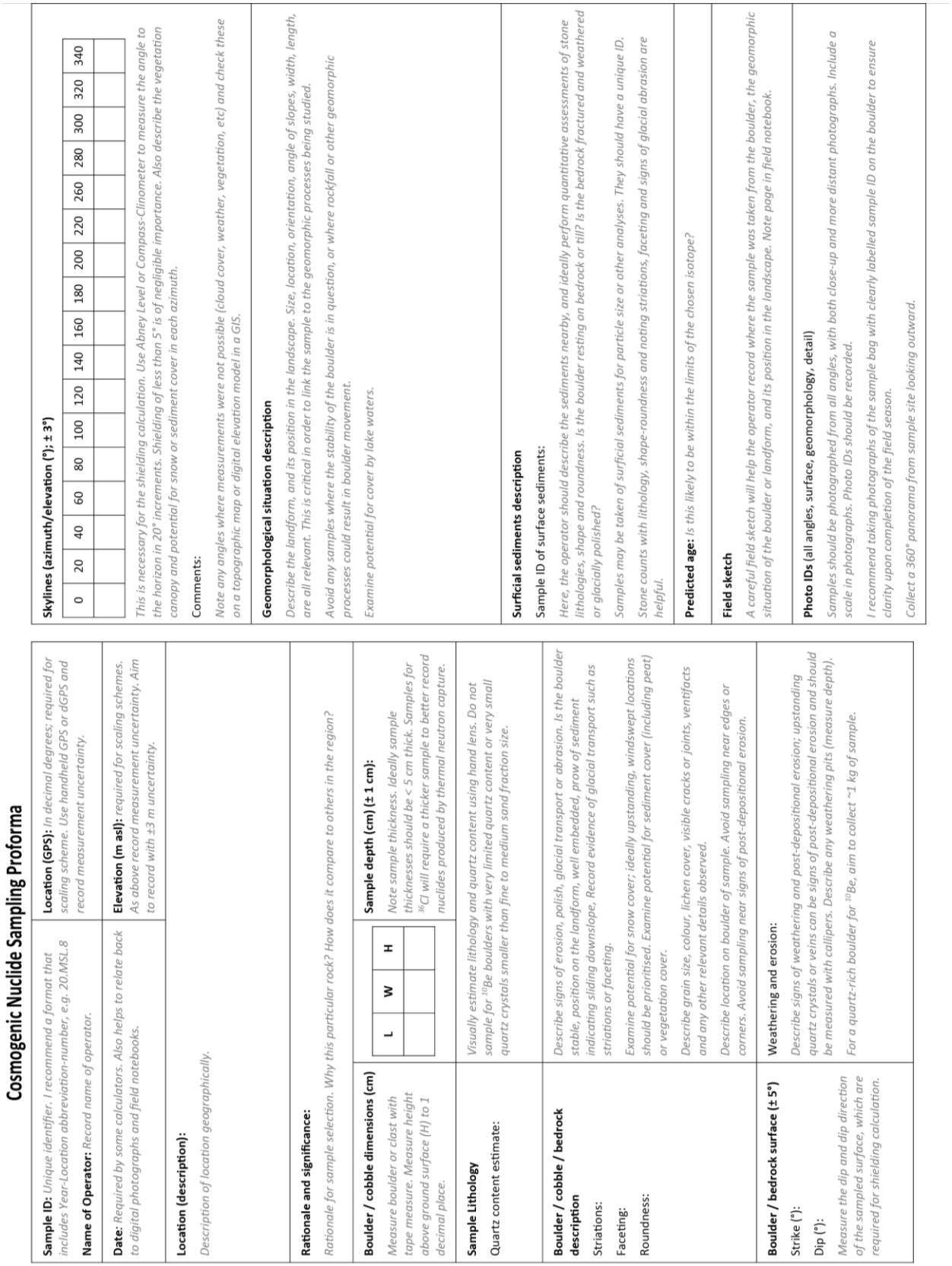

Cosmogenic Nuclide Sampling Proforma

Sample ID: *Unique identifier. I recommend a format that includes Year-Location abbreviation-number, e.g. 20.MSL.8*

Name of Operator: *Record name of operator.*

Location (GPS): *In decimal degrees; required for scaling scheme. Use handheld GPS or dGPS and record measurement uncertainty.*

Date: *Required by some calculators. Also helps to relate back to digital photographs and field notebooks.*

Elevation (m asl): *required for scaling schemes. As above record measurement uncertainty. Aim to record with ±3 m uncertainty.*

Location (description):

Description of location geographically.

Rationale and significance:

Rationale for sample selection. Why this particular rock? How does it compare to others in the region?

Boulder / cobble dimensions (cm)

Measure boulder or clast with tape measure. Measure height above ground surface (H) to 1 decimal place.

L	W	H

Sample depth (cm) (± 1 cm):

Note sample thickness. Ideally sample thicknesses should be < 5 cm thick. Samples for ^{36}Cl will require a thicker sample to better record nuclides produced by thermal neutron capture.

Sample Lithology

Quartz content estimate:

Visually estimate lithology and quartz content using hand lens. Do not sample for ^{10}Be boulders with very limited quartz content or very small quartz crystals smaller than fine to medium sand fraction size.

Boulder / cobble / bedrock description

Striations:

Faceting:

Roundness:

Describe signs of erosion, polish, glacial transport or abrasion. Is the boulder stable, position on the landform, well embedded, prow of sediment indicating sliding downslope, Record evidence of glacial transport such as striations or faceting.

Examine potential for snow cover; ideally upstanding, windswept locations should be prioritised. Examine potential for sediment cover (including peat) or vegetation cover.

Describe grain size, colour, lichen cover, visible cracks or joints, ventifacts and any other relevant details observed.

Describe location on boulder of sample. Avoid sampling near edges or corners. Avoid sampling near signs of post-depositional erosion.

Boulder / bedrock surface (± 5°)

Strike (°):

Dip (°):

Measure the dip and dip direction of the sampled surface, which are required for shielding calculation.

Weathering and erosion:

Describe signs of weathering and post-depositional erosion; upstanding quartz crystals or veins can be signs of post-depositional erosion and should be measured with callipers. Describe any weathering pits (measure depth).

For a quartz-rich boulder for ^{10}Be, aim to collect ~1 kg of sample.

Skylines (azimuth/elevation (°); ± 3°)

0	20	40	60	80	100	120	140	160	180	200	220	260	280	300	320	340

This is necessary for the shielding calculation. Use Abney Level or Compass-Clinometer to measure the angle to the horizon in 20° increments. Shielding of less than 5° is of negligible importance. Also describe the vegetation canopy and potential for snow or sediment cover in each azimuth.

Comments:

Note any angles where measurements were not possible (cloud cover, weather, vegetation, etc) and check these on a topographic map or digital elevation model in a GIS.

Geomorphological situation description

Describe the landform, and its position in the landscape. Size, location, orientation, angle of slopes, width, length, are all relevant. This is critical in order to link the sample to the geomorphic processes being studied.

Avoid any samples where the stability of the boulder is in question, or where rockfall or other geomorphic processes could result in boulder movement.

Examine potential for cover by lake waters.

Surficial sediments description

Sample ID of surface sediments:

Here, the operator should describe the sediments nearby, and ideally perform quantitative assessments of stone lithologies, shape and roundness. Is the boulder resting on bedrock or till? Is the bedrock fractured and weathered or glacially polished?

Samples may be taken of surficial sediments for particle size or other analyses. They should have a unique ID.

Stone counts with lithology, shape-roundness and noting striations, faceting and signs of glacial abrasion are helpful.

Predicted age: *Is this likely to be within the limits of the chosen isotope?*

Field sketch

A careful field sketch will help the operator record where the sample was taken from the boulder, the geomorphic situation of the boulder or landform, and its position in the landscape. Note page in field notebook.

Photo IDs (all angles, surface, geomorphology, detail)

Samples should be photographed from all angles, with both close-up and more distant photographs. Include a scale in photographs. Photo IDs should be recorded.

I recommend taking photographs of the sample bag with clearly labelled sample ID on the boulder to ensure clarity upon completion of the field season.

Collect a 360° panorama from sample site looking outward.

Figure 7. Example of a sampling proforma for sampling boulders, cobbles or bedrock for exposure ages. Notes for field workers are shown in grey text. Using a sampling proforma limits the chance of critical information being missed or not collected in the field. GPS: Geographic Positioning System. dGPS: Differential GPS.

Figure 8. Examples of boulders sampled for cosmogenic nuclide dating. A, B: Granite erratic boulders on moraines in Patagonia (Davies et al., 2018; Thorndycraft et al., 2019). C: Erratic granite boulder on moraine, James Ross Island. D: Well embedded granite erratic boulder at Ablation Point Massif, Alexander Island, Antarctic Peninsula (Davies et al., 2017). E: Sandstone boulder on moraine ridge crest, Ablation Point Massif, Alexander Island (Davies et al., 2017). F: Granite erratic boulder on Carboniferous sandstone bedrock, James Ross Island, Antarctic Peninsula (Glasser et al., 2014).

3.4.2 Burial dating sampling methodologies

Sampling methodologies are outlined in Gosse and Phillips (2001). Much of the discussion for sampling boulders or bedrock for exposure ages also applies to depth profiles of allochthonous sediments. However, sediments may contain clasts with a previous exposure and so have an inheritance. Clast cycling within the active layer, bioturbation and pedoturbation may cause vertical mixing (Gosse and Phillips, 2001; Ivy-Ochs et al., 2013). Depth profiles should be sampled where sedimentary analysis suggests no mixing (e.g., original fluvial bedding structures, soil horizons). Samples should be taken below rooting depth in forested surfaces. Areas of high relief such as knolls, or depressions, should be avoided.

Samples are taken through a deep (e.g. >1.5 m) exposure in the sedimentary unit, either as bulk mixtures or selected lithologies (e.g. targeting quartz-rich clasts or sand). Selecting fractions greater than sand-size may affect profile modelling (Hidy et al., 2010). The method assumes that the unit was deposited in a single geologic event, and that nuclide accumulation through the sediments attenuates with depth (Anderson et al., 1996; Repka et al., 1997).

3.5 Reporting and analysing cosmogenic nuclide data

3.5.1 Calculating and presenting cosmogenic nuclide ages

A number of calculators are available for the calculation of cosmogenic nuclide ages. These presently include IceTEA (Jones et al., 2019), CREp (Martin et al., 2017) and the online calculators formerly known as the CRONUS-Earth online calculators (Balco et al., 2008; Marrero et al., 2016a; Phillips et al., 2016). These calculators allow for the selection of various scaling schemes and production rates and allow cosmogenic nuclide ages to be easily recalculated. These calculators require that data is formatted in a particular way. Essential required data include sample ID, AMS standard, $^{10}Be/^{9}Be$ ratio, latitude, longitude, altitude, AMS measurement of nuclide concentration and measurement uncertainty, sample thickness, shielding, sample density, erosion rate, and date of sample collection (Balco, 2011; Balco et al., 2008; Dunai and Stuart, 2009; Gosse and Phillips, 2001). The practitioner should present and justify their chosen production rate and scaling scheme. These data will allow readers to recalibrate ages with different production rates or scaling schemes. The practitioner should explain their chosen erosion rate, and ideally present results with a zero erosion rate as well as any other erosion rate used. Any other corrections used (e.g. snow cover) should also be explained and evaluated. Elevation change due to isostatic uplift may be a significant cause of age variation, and can be taken into account by some calculators (such as IceTEA, Jones et al., 2019).

Exposure-age calculators will produce *internal* and *external* uncertainties. Both should be presented. Internal uncertainties are those only associated with the measurement error in the nuclide concentration. They are the same for all scaling schemes (Balco, 2011; Balco et al., 2008). External uncertainties include those corresponding to the production rate and scaling scheme, with production rate sites that may be hundreds to thousands of kilometres apart and elevational scaling over thousands of metres. External uncertainties are systematic when all cosmogenic nuclide data is processed in the same way, and so exposure ages can be compared within a given area using internal uncertainties. However, when comparing exposure age data to other independent dating methods (such as radiocarbon dating), external uncertainties should be used.

3.5.2 Statistical treatment of outliers

There is a wide range of tools available for practitioners to deal with outliers, summarized in Balco (2011) and Jones et al. (2019). In cases where inheritance is an expected issue, such as polar environments, excluding anomalously old ages may be sufficient (Bentley et al., 2006; Hein et al., 2016). Inheritance can also be screened for using a co-isotope plot, and boulders with a complex exposure history excluded in this way (cf. Balco, 2011; Bentley et al., 2006; Corbett et al., 2013). Alternatively, if processes such as exhumation and moraine degradation are considered to be more important, imparting a young bias, excluding anomalously young ages may be more appropriate (Putkonen and Swanson, 2003).

Cosmogenic nuclide exposure ages are frequently presented on Gaussian (normal) probability density functions or kernel density estimates (sometimes known as 'camel plots') (Balco, 2009; Chevalier et al., 2011; Darvill et al., 2018; Davies et al., 2019; Jones et al., 2019; Joy et al., 2014; Kaplan et al., 2020; Putnam et al., 2010; Schimmelpfennig et al., 2014; Spencer et al., 2017). These plots present a Gaussian for each sample with mean and standard deviation. The area under the curve is the same for each sample, so the narrower and higher the peak, the more precise the age measurement. The height of the curve is inversely proportional to the measurement uncertainty. These plots can be useful for describing the frequency distribution of observations, and for visual identification of outliers without overlapping uncertainties, for a particular landform such as a moraine.

They can be summed to present a summary curve. If the summary curve has only one discrete peak, then the age measurements for the landform dated are both inaccurate measurements of the same thing (e.g. Figure 9). If the data do not agree within their uncertainties, then the summed Gaussian plot may have two or more peaks, which can highlight geological scatter and aid outlier identification (Jones et al., 2019).

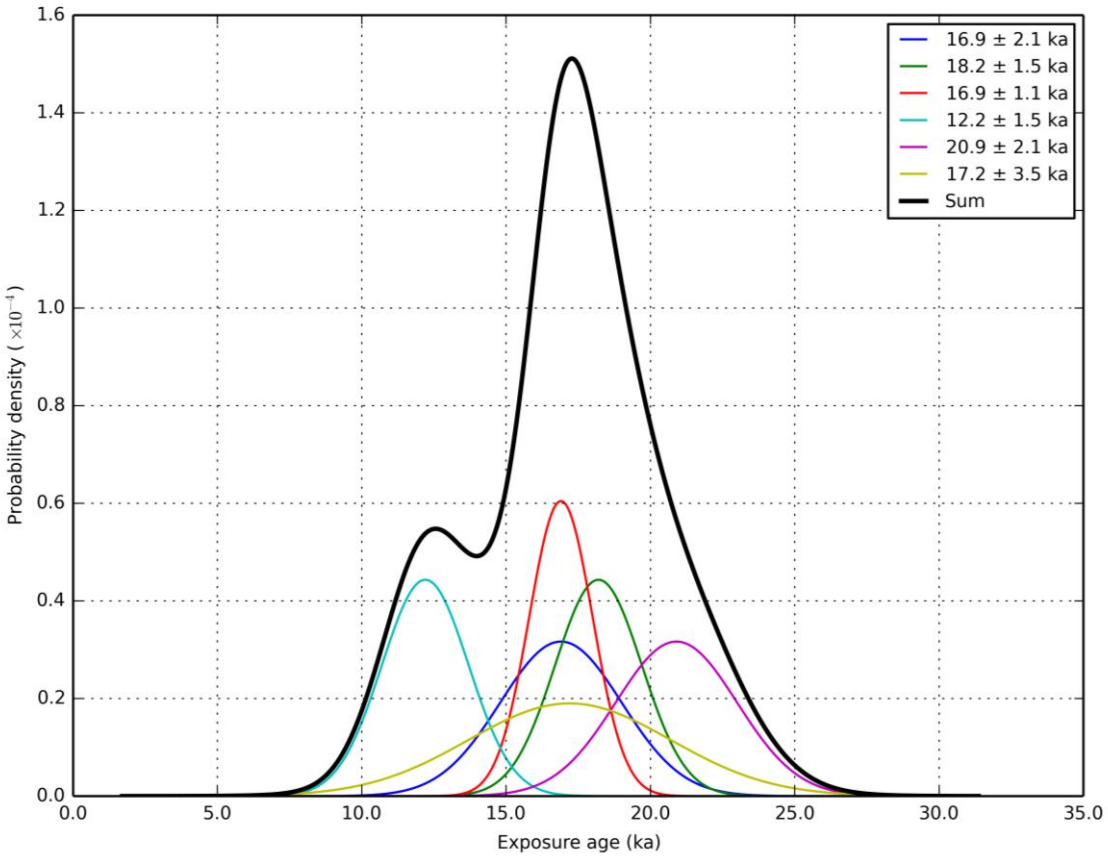

Figure 9. Example Gaussian probability density functions for several ages from northern England, Britain (ages from Davies et al., 2019)*. Coloured lines are individual ages and the black line is the summed probability curve. The summed plot highlights that the age of 12.2 ± 1.5 ka is an outlier.*

Balco (2011) and Jones et al. (2019) provide further criteria for the identification of outliers from single landforms such as moraines. These include a reduced chi-squared statistic. The expected value of this is 1 if measurement uncertainty is the only source of scatter (Balco, 2011). However, most exposure-age datasets from temperate glacier moraines have chi-squared values greater than 1, indicating that it is unlikely that measurement uncertainty is the only source of scatter. Other tests that have been applied include Chauvenet's criterion (Rinterknecht et al., 2006), Grubb's Test (Putnam et al., 2010) or assessments of data skew (Applegate et al., 2010). Jones et al. (2019) provide a series of statistical tools in the IceTEA calculator to identify outliers, including a two-tailed generalised extreme Studentized deviate (gESD) test. This test can account for multiple outliers.

Finally, Bayesian age modelling also provides a means to test for outliers by including a series of dated moraine margins that can be placed into an order using the concept of morphostratigraphy, proximity to the ice divide, or independent age measurements. This method assumes that ages take place within a spatial and temporal framework (Chiverrell et al., 2013; Laabs et al., 2013, 2007; Small et al., 2017; Thorndycraft et al., 2019). It assumes, for example, that outer moraines are older than inner moraines, and allows for an independently constructed sequence of events (a 'prior' model). Bayesian age modelling of this kind robustly handles outliers, and can reduce modelled age uncertainties. It can be used for surface exposure ages, bracketing radiocarbon ages or other chronological tools, and different tools can be integrated together (Blockley et al., 2007; Bronk Ramsey, 2009; Buck et al., 1996).

3.5.3 Moraine mean ages

Where multiple boulders from a moraine have been analysed for cosmogenic nuclide analysis, and outliers have been excluded, it is often desirable to produce a mean age for the moraine. If measurement errors for individual ages are independent and normally distributed, as is the case for analytical measurements, then scatter due to measurement uncertainty can be eliminated by averaging multiple ages (Balco, 2011). The mean of many cosmogenic nuclide measurements will yield a more accurate and precise landform age than one age alone. There are multiple ways to do this: giving the full age range of the boulders on the moraine, a mean age with a standard deviation, and uncertainty weighted means (Applegate et al., 2012).

Uncertainty weighted means are commonly used to summarise data, where the mean age of the landform with an uncertainty based on the measured uncertainty from each sample is calculated (Jones et al., 2019; Rinterknecht et al., 2008; Schaefer et al., 2009). Uncertainty weighted means may be appropriate on samples that have a reduced chi-squared statistic that suggests that scatter is due to measurement uncertainty alone (Balco, 2011).

Uncertainty weighted means can however be problematic (cf. Davies et al., 2020). As most of the uncertainty on the individual ages comes from the uncertainties in the production rate and scaling scheme, the uncertainties of the ages within the same group of samples from the same region are usually quite homogeneous. Further, the scatter of the ages within the same group is typically higher than the individual age uncertainties, suggesting that the natural "noise" in the ^{10}Be ages due to the geological characterisation of the samples (i.e. position on the moraine, weathering, flaking, exhumation and denudation) is higher than the uncertainties considered in the age calculations (laboratory systematic errors, AMS precision, production rate and scaling uncertainties). Older moraines may be especially susceptible to these issues, where erosion may be more statistically important and where uncertainties in age calculations are higher. Therefore, the calculated mean ages and standard deviations represent landform ages better than uncertainty weighted means. In addition, different samples may be more or less difficult to process in the laboratory; for instance, having more or less non-quartz minerals. This leads to samples having different precision on their measurements, but this is not reflective of sample quality (i.e. position on moraine, weathering, flaking, exhumation or denudation). In an uncertainty weighted mean, this would disproportionately weight the mean in a non-accurate way.

A simpler way to reduce the data is to firstly, exclude outliers, and secondly, to provide the arithmetic mean landform age (μ) and the standard deviation (1σ), which gives an indication of the spread of ages on the landform (Davies et al., 2020; Nimick et al., 2016). This should only use high quality ages that pass the quality assurance protocols (below), and exclude outliers without overlapping uncertainties at 2σ. This can reduce and simplify the data, and can facilitate inter-regional comparisons. It also allows an assessment of the spread of ages on the landform, without being biased by measurement uncertainty.

Moraine or landform mean ages should be presented with a standard deviation in the format following standard protocols (Curran-Everett and Benos, 2004; Davies et al., 2020; Ludbrook, 2008) with the age and unit, and the standard deviation in brackets after. For example, presented as 5.2 ka (SD 0.5). They should not use a plus and minus sign, as the standard deviation is always positive and does not represent uncertainty, only a spread of the ages. Individual ages with a measured uncertainty around the age should be presented as, for example, 5.2 ± 0.5 ka. Weighted means with a weighted uncertainty estimate should also be presented as 5.2 ± 0.5 ka.

3.6 Cosmogenic nuclide quality assurance protocols

High quality cosmogenic nuclide surface-exposure ages should sample multiple (ideally 3 or more) replicate boulders from the same landform from each site. Outliers should be assessed and identified. The ages should be internally consistent, with a spread of ages similar to the measurement uncertainty. The data to recalibrate ages using the latest published calibration models should be provided. Geological and geomorphological context should be clear and ideally field sample photographs provided so that the reader can assess their suitability for dating.

High quality cosmogenic depth profiles should have a modelled profile age compared to separate surface cobble ages. There should be multiple samples in a profile (ideally ≥5), including at least one sample >1.5 m deep. High quality profiles would have ages that are internally consistent and clustered. The geomorphological situation should be accounted for; this should include that any terraces stabilised shortly after moraine stabilisation, that the nuclide inheritance is low, that post-depositional shielding is minimal, and that terrace sediment is not mixed post-depositionally.

4 Optically stimulated luminescence (OSL)

4.1 Principles of OSL dating

Luminescence dating can directly determine the time since a mineral grain was last deposited and buried. It quantifies the time since mineral grains were last exposed to sunlight (Small et al., 2017). It can be applied to sediments from decades old to up to 200,000 years old (Smedley, 2018). Strengths of the technique include that it can directly determine the time since sediment burial across a wide range of depositional settings, and that it can date dust, sands and rocks. Numerous detailed reviews are available (Lian, 2013; Lowe and Walker, 2014; Rhodes, 2011; Smedley, 2018; Smedley et al., 2019; Stokes, 1999), so principles are discussed only briefly here.

The technique relies upon the ability of quartz or K-feldspar grains to store energy within the crystal structure and release it when stimulated using light (optically stimulated luminescence; OSL) or heat (thermoluminescence; TL). During transport, grains are exposed to sunlight, which releases the accumulated charge within the crystal lattice. After burial, grains are exposed to ionising radiation from radioactive elements naturally occurring within the sediment (U, Th, K and Rb), and from cosmic rays. This ionising radiation excites the electrons, which then become trapped within crystal imperfections (electron traps) in the crystal lattice (Lian, 2013; Small et al., 2017). The rate at which electrons are accumulated is termed the "environmental dose rate". The total dose to which the grains were exposed to during burial (the "equivalent dose") can be determined in the laboratory, and divided by the environmental dose rate, to determine the time since deposition.

Luminescence dating is best applied in settings where grains are well-bleached during transport (e.g. aeolian). In glacial settings, the luminescence signal is typically partially bleached, where sediments are transported rapidly and over short distances, in environments such as turbid, sediment-laden meltwater flow (Smedley and Skirrow, 2020). Compared with sands deposited as part of a moraine, glaciofluvial sediments maximise the opportunity for bleaching, but the OSL signals of individual grains are still typically incompletely bleached prior to burial (King et al., 2014). The development of the single-aliquot regenerative

(SAR) protocol (Murray and Wintle, 2000) has allowed OSL to be used in glaciofluvial settings (Duller, 2006; Glasser et al., 2006). Single grain optical dating allows for statistical analysis and rejection of grains that have incomplete bleaching, allowing the age of the sample to be determined. Single-grain analysis dramatically improves the accuracy of luminescence ages for partially bleached sediments (Smedley, 2018).

OSL is most frequently applied to quartz and feldspar, as these minerals are ubiquitous in sedimentary environments. Quartz is often preferred, as it bleaches more rapidly in sunlight than the post-IR IRSL signal of K-feldspar (Smedley et al., 2019). However, K-feldspars in glaciofluvial environments may be more efficient than quartz at determining the population of interest for age calculations. Commonly, only 5% or fewer grains of quartz emit a detectable OSL signal, and in some environments, such as glaciofluvial environments in Chile, fewer than 0.5% of quartz grains could be detected (Duller, 2006; Smedley et al., 2016). In these environments, a larger proportion of K-feldspar grains emit a detectable infra-red stimulated luminescence (IRSL) signal (Smedley et al., 2016; Smedley and Pearce, 2016). As a result, K-feldspar single-grain dating may make luminescence dating more efficient and precise in areas characterised by short sediment transport pathways of where the sensitivity of quartz is poor. Dating feldspars also has the potential to extend further back in time than OSL dating of quartz grains (Smedley, 2018). However, K-feldspars are prone to anomalous fading, which can lead to an underestimation of the burial age (Smedley et al., 2016). Protocols for this are outlined in several publications, which detail how to account for fading (Huntley and Lamothe, 2001), or methods for determination using more stable signals such as the post-IR IRSL signal in K-feldspars (Thomsen et al., 2011, 2008).

Dose Rate calculators such as DRAC (Dose Rate and Age Calculator) provides an open-access, web-based program that enables rapid calculation of dose rates (Durcan et al., 2015). This facilitates inter-laboratory comparisons and enables easier dose-rate calculations.

4.2 Application in glacial environments

Direct dating of sands deposited by ice masses (e.g. within till or moraines) is challenging due to the likelihood of impartial bleaching. However, in glacial settings, OSL applied to glacial outwash sediments that can be directly linked to a moraine can constrain the position of the ice margin when it was at that moraine (Harrison et al., 2012; Smedley et al., 2016), or can be used to date perched deltas associated with ice-dammed palaeolakes (Glasser et al., 2016). OSL ages from sands directly above or below glacial sediments can also provide bracketing ages for a glacial event (Bateman et al., 2015).

Sources of uncertainty in glacial environments for OSL dating include partial bleaching and resetting of the OSL signal during transportation and deposition (King et al., 2014; Small et al., 2017). This should be addressed using small multi-grain aliquots or single aliquots; standard aliquots of ~2500 grains can average out the effects of variable grain bleaching (Duller, 2008). Large numbers of replicate measurements and statistical analysis can be used to characterise the distribution and diagnose the presence of partial bleaching (Small et al., 2017).

In recent years, practitioners have used OSL to date buried clasts in sizes from centimetres to decimetres in diameter (Sohbati et al., 2012). This has advantages in that water content variability can be excluded, and the degree of bleaching that occurred before burial can be assessed using data from the rock sample itself (Jenkins et al., 2018). In glacial environments, where partial bleaching is a common challenge, OSL dating of cobbles may allow more straightforward interpretations of past bleaching history. New methods are

developing that use OSL principles in rock cores drilled in granite cobbles on glaciofluvial outwash fans (Jenkins et al., 2018). Grains within the rocks were completely bleached to a depth of 12 mm.

4.3 OSL Sampling Strategies

A sampling strategy must take careful note of depositional environments and the geomorphic context in order to ensure the most appropriate samples are taken. Samples are usually taken by inserting opaque plastic tubes into a cleaned section face (Lian, 2013). The container is excavated and sealed. This can be done under a black tarpaulin to ensure no light penetrates the tube. Samples can also be carved out in cohesive blocks, and wrapped in aluminium foil for protection. Typically, around 1 kg of sample is required. For sampling cobbles in glaciofluvial sands, orientated cobbles from bar-top depositional environments are most appropriate for sampling (Jenkins et al., 2018).

4.4 Optically Stimulated Luminescence dating quality assurance protocols

High quality optically stimulated luminescence ages would ensure that any potential for partial bleaching has been addressed by using small aliquot or single grain measurements. The stratigraphic context should be well understood, and proglacial outwash can be directly linked to a moraine or ice marginal position. There should be multiple or stratigraphically consistent ages, and dose rate information and equivalent described in the source. The age should not be determined using an experimental analysis protocol.

5 K/Ar and Ar/Ar ages

$^{40}Ar/^{39}Ar$ dating of basaltic lava sequences interbedded with moraines can provide a chronological framework for dating moraines. The technique is based on the radioactive decay of ^{40}K to ^{40}Ar. In most studies, the derivative $^{40}Ar/^{39}Ar$ method is used, where ^{39}Ar is used as a proxy for ^{40}K. This allows for smaller single aliquot samples (Briner, 2011; Jull, 2018; Wijbrans and Kuiper, 2013). This method can be applied to sediments that are very young (~24 ka) (Turrin et al., 2007) to those that are billions of years old. It is usually applied to K-rich volcanic rocks. Dating of moraine sequences by dating the overlapping and interbedded lava flows using Ar/Ar (e.g., Singer et al., 2004a, 2004b) could be considered indirect dating by providing bracketing ages.

In Patagonia, older Mid Pleistocene moraines interbedded with lava flows were dated with bracketing $^{40}Ar/^{39}Ar$ ages (Singer et al., 2004a). These ages date basalt lava flows from Cerro Volcán to 760 ± 14 ka and 109 ± 3 ka, with the older age underlying six moraines, and the older age overlying and burying the moraines. In Hawaii, K-Ar dating of lava flows that underlie and overlie glacial sediments provided bracketing ages for the glacial advances (Porter, 2005).

6 Summary and conclusions

This chapter has summarized the application of radiometric methods (cosmogenic nuclide dating, radiocarbon dating, optically stimulated luminescence dating, argon-argon and potassium-argon dating) to glacial environments. These numerical radiometric techniques can be used in conjunction with archival

methods, relative dating methods such as morphostratigraphy and Schmidt hammer dating, and incremental methodologies such as lichenometry, varve counting and dendroglaciology to date glacial landforms across a wide range of different glacial environments and different timescales.

The rapid pace of developments in radiometric dating glacial landforms provides glacial geologists a powerful toolbox for fixing in time past glacier-climate interactions. Dating features such as moraines allows the timing of significant stabilisations of outlet glaciers to be characterized. All of these dating techniques rely upon a sound understanding of the regional glacial geomorphology and geology, and must be underpinned by a thorough geomorphological mapping campaign that seeks to understand the morphometric and stratigraphic relationships between landforms. Chronologies should be constructed with adherence to quality assurance protocols, which also allow tools for the analysis and comparison of new datasets to legacy data. Outliers can be assessed using a range of tools, including Bayesian age modelling, which allows chronologies to be built from different dating methods if depositional contexts are sufficiently understood to build a 'prior' model. These methods together can be applied to derive highly confident mean age estimates for glacial landforms.

Careful application of these methodologies, together with improving understanding of their assumptions and limitations, and improving protocols for sample selection, laboratory analysis, age calculation and identification and treatment of outliers, has resulted in large datasets for every ice sheet. Compilations of these geomorphological and chronological data, together with an understanding of their age reliability, now allow an unprecedented view into past ice-sheet behavior through time (Batchelor et al., 2019; Dalton et al., 2020; Davies et al., 2020; Hughes et al., 2016; Margold et al., 2018; Ó Cofaigh et al., 2014). These datasets highlight key gaps in knowledge and can emphasise priorities for future research, evaluate regional disparities, and calculate regional rates of horizontal and vertical recession (Davies et al., 2020).

Robust glacial chronologies using numerical ages that can be used to carefully correlate ice extents over wide regional areas are vital to understand past ice sheet or glacier response to palaeoclimate. Integration of these empirical datasets with numerical simulations requires a robust treatment of uncertainties. These empirical datasets are increasingly used to calibrate numerical simulations (Albrecht et al., 2020a; Golledge et al., 2014; Patton et al., 2016, 2017; Stokes and Tarasov, 2010) and define ice-ocean-atmosphere interactions by linking ice flow and mass balance with ice extent and thickness data (Albrecht et al., 2020a, 2020b; Ely et al., 2019; Gandy et al., 2019). These exciting developments herald a new understanding in ice mass response to external drivers of change (ocean and atmospheric temperatures) compared with internal drivers, such as ice divide migration, topography, calving, or ice-dammed proglacial lakes. These efforts will help to understand likely drivers of change in current ice masses, and future rates and magnitudes of sea level change, mountain glacier recession and meltwater supply, and changing glacier-related hazards. Large empirical datasets of geomorphology and carefully collected and analysed chronological data, grounded in a thorough understanding of glacial process, is critical to this effort.

Relevant Websites

- https://hess.ess.washington.edu/ (accessed on 01.02.2020). *The online calculators formerly known as the CRONUS-Earth online calculators*
- http://ice-tea.org/en/ (accessed on 01.02.2020). *Tools for Exposure Ages from ice margins*
- http://calibration.ice-d.org/ (accessed on 30.03.2020). Production rate calibration data.

- https://c14.arch.ox.ac.uk/oxcal.html (accessed on 01.02.2020). A tool for radiocarbon calibration.
- http://calib.org/calib/ (accessed on 01.02.2020). A tool for radiocarbon calibration.
- http://calib.org/marine (accessed on 31.10.2020). A database of global Δ*R* values.
- https://www.aber.ac.uk/en/dges/research/quaternary/luminescence-research-laboratory/dose-rate-calculator/ (accessed on 06.04.2020). Dose Rate Calculator for OSL dating (*DRAC*).

Acknowledgements

Davies acknowledges Malcolm Kelsey for assistance in producing some of the figures and graphics. Davies acknowledges fruitful discussions with many colleagues over several years that aided the development of the quality assurance protocols, methods for analyzing and presenting chronological data, and all colleagues who contributed to remote, challenging fieldwork and the gathering of datasets.

List of Figures

List of Tables

References

Albrecht, T., Winkelmann, R., Levermann, A., 2020a. Glacial-cycle simulations of the Antarctic Ice Sheet with the Parallel Ice Sheet Model (PISM)–Part 2: Parameter ensemble analysis. Cryosph. 14, 633–656.

Albrecht, T., Winkelmann, R., Levermann, A., 2020b. Glacial-cycle simulations of the Antarctic Ice Sheet with the Parallel Ice Sheet Model (PISM)-Part 1: Boundary conditions and climatic forcing. Cryosph. 14, 599.

Alves, E.Q., Macario, K., Ascough, P., Bronk Ramsey, C., 2018. The Worldwide Marine Radiocarbon Reservoir Effect: Definitions, Mechanisms, and Prospects. Rev. Geophys. 56, 278–305. https://doi.org/10.1002/2017RG000588

Anderson, R.S., Repka, J.L., Dick, G.S., 1996. Explicit treatment of inheritance in dating depositional surfaces using in situ ^{10}Be and ^{26}Al. Geology 24, 47–51.

André, M., 2002. Rates of postglacial rock weathering on glacially scoured outcrops (abisko–riksgränsen area, 68°n). Geogr. Ann. Ser. A, Phys. Geogr. 84, 139–150. https://doi.org/10.1111/j.0435-3676.2002.00168.x

Andrews, J.T., Domack, E.W., Cunningham, W.L., Leventer, A., Licht, K.J., Jull, A.J.T., DeMaster, D.J., Jennings, A.E., 1999. Problems and Possible Solutions Concerning Radiocarbon Dating of Surface Marine Sediments, Ross Sea, Antarctica. Quat. Res. 52, 206–216. https://doi.org/http://dx.doi.org/10.1006/qres.1999.2047

Applegate, P.J., Urban, N.M., Keller, K., Lowell, T. V, Laabs, B.J.C., Kelly, M.A., Alley, R.B., 2012. Improved moraine age interpretations through explicit matching of geomorphic process models to cosmogenic nuclide measurements from single landforms. Quat. Res. 77, 293–304. https://doi.org/http://dx.doi.org/10.1016/j.yqres.2011.12.002

Applegate, P.J., Urban, N.M., Laabs, B.J.C., Keller, K., Alley, R.B., 2010. Modeling the statistical distributions of cosmogenic exposure dates from moraines. Geosci. Model Dev. 3, 293–307. https://doi.org/10.5194/gmd-3-293-2010

Balco, G., 2020. Technical note: A prototype transparent-middle-layer data management and analysis infrastructure for cosmogenic-nuclide exposure dating. Geochronol. Discuss. 2020, 1–10. https://doi.org/10.5194/gchron-2020-6

Balco, G., 2014. Simple computer code for estimating cosmic-ray shielding by oddly shaped objects. Quat. Geochronol. 22, 175–182.

Balco, G., 2011. Contributions and unrealized potential contributions of cosmogenic-nuclide exposure dating to glacier chronology, 1990 - 2010. Quat. Sci. Rev. 30, 3–27. https://doi.org/http://dx.doi.org/10.1016/j.quascirev.2010.11.003

Balco, G., 2009. MATLAB code for camel diagrams [WWW Document]. URL https://cosmognosis.wordpress.com/2009/07/13/matlab-code-for-camel-diagrams/ (accessed 4.2.20).

Balco, G., Briner, J., Finkel, R.C., Rayburn, J.A., Ridge, J.C., Schaefer, J.M., 2009. Regional beryllium-10 production rate calibration for late-glacial northeastern North America. Quat. Geochronol. 4, 93–107.

Balco, G., Rovey, C.W., 2008. An isochron method for cosmogenic-nuclide dating of buried soils and sediments. Am. J. Sci. 308, 1083–1114.

Balco, G., Stone, J.O., Lifton, N.A., Dunai, T.J., 2008. A complete and easily accessible means of calculating surface exposure ages or erosion rates from ^{10}Be and ^{26}Al measurements. Quat. Geochronol. 3, 174–195.

Balco, G.A., Schaefer, J.M., Group, L., 2013. Terrestrial exposure-age record of Holocene ice sheet and ice-shelf change in the northeast Antarctic Peninsula. Quat. Sci. Rev. 59, 101–111.

Batchelor, C.L., Margold, M., Krapp, M., Murton, D.K., Dalton, A.S., Gibbard, P.L., Stokes, C.R., Murton, J.B., Manica, A., 2019. The configuration of Northern Hemisphere ice sheets through the Quaternary. Nat. Commun. 10, 3713. https://doi.org/10.1038/s41467-019-11601-2

Bateman, M.D., Evans, D.J.A., Buckland, P.C., Connell, E.R., Friend, R.J., Hartmann, D., Moxon, H., Fairburn, W.A., Panagiotakopulu, E., Ashurst, R.A., 2015. Last glacial dynamics of the Vale of York and North Sea lobes of the British and Irish Ice Sheet. Proc. Geol. Assoc. 126, 712–730. https://doi.org/http://dx.doi.org/10.1016/j.pgeola.2015.09.005

Bateman, M.D., Evans, D.J.A., Roberts, D.H., Medialdea, A., Ely, J., Clark, C.D., 2018. The timing and consequences of the blockage of the Humber Gap by the last British− Irish Ice Sheet. Boreas 47, 41–61.

Bentley, M.J., Fogwill, C.J., Kubnik, P.W., Sugden, D.E., 2006. Geomorphological evidence and cosmogenic $^{10}Be/^{26}AL$ exposure ages for the Last Glacial Maximum and deglaciation of the Antarctic Peninsula Ice Sheet. GSA Bull. 118, 1149–1159. https://doi.org/DOI: 10.1130/B25735.1

Bentley, M.J., Fogwill, C.J., Le Brocq, A.M., Hubbard, A.L., Sugden, D.E., Dunai, T.J., Freeman, S.P.H.T., 2010. Deglacial history of the West Antarctic Ice Sheet in the Weddell Sea embayment: Constraints on past ice volume change. Geology 38, 411–414. https://doi.org/DOI: 10.1130/g30754.1

Bentley, M.J., Johnson, J.S., Hodgson, D.A., Dunai, T., Freeman, S.P.H.T., Ó Cofaigh, C., 2011. Rapid deglaciation of Marguerite Bay, western Antarctic Peninsula in the Early Holocene. Quat. Sci. Rev. 30, 3338–3349.

Bentley, M.J., Ó Cofaigh, C., Anderson, J.B., Conway, H., Davies, B., Graham, A.G.C., Hillenbrand, C.-D., Hodgson, D.A., Jamieson, S.S.R., Larter, R.D., Mackintosh, A., Smith, J.A., Verleyen, E., Ackert, R.P., Bart, P.J., Berg, S., Brunstein, D., Canals, M., Colhoun, E.A., Crosta, X., Dickens, W.A., Domack, E., Dowdeswell, J.A., Dunbar, R., Ehrmann, W., Evans, J., Favier, V., Fink, D., Fogwill, C.J., Glasser, N.F., Gohl, K., Golledge, N.R., Goodwin, I., Gore, D.B., Greenwood, S.L., Hall, B.L., Hall, K., Hedding, D.W., Hein, A.S., Hocking, E.P., Jakobsson, M., Johnson, J.S., Jomelli, V., Jones, R.S., Klages, J.P., Kristoffersen, Y., Kuhn, G., Leventer, A., Licht, K., Lilly, K., Lindow, J., Livingstone, S.J., Massé, G., McGlone, M.S., McKay, R.M., Melles, M., Miura, H., Mulvaney, R., Nel, W., Nitsche, F.O., O'Brien, P.E., Post, A.L., Roberts, S.J., Saunders, K.M., Selkirk, P.M., Simms, A.R., Spiegel, C., Stolldorf, T.D., Sugden, D.E., van der Putten, N., van Ommen, T., Verfaillie, D., Vyverman, W., Wagner, B., White, D.A., Witus, A.E., Zwartz, D., 2014. A community-based geological reconstruction of Antarctic Ice Sheet deglaciation since the Last Glacial Maximum. Quat. Sci. Rev. 100. https://doi.org/10.1016/j.quascirev.2014.06.025

Blockley, S.P.E., Blaauw, M., Ramsey, C.B., van der Plicht, J., Bronk Ramsey, C., van der Plicht, J., 2007. Building and testing age models for radiocarbon dates in Lateglacial and Early Holocene sediments. Quat. Sci. Rev. 26, 1915–1926. https://doi.org/http://dx.doi.org/10.1016/j.quascirev.2007.06.007

Boex, J., Fogwill, C., Harrison, S., Glasser, N.F., Hein, A., Schnabel, C., Xu, S., 2013. Rapid thinning of the late Pleistocene Patagonian Ice Sheet followed migration of the Southern Westerlies. Sci. Rep. 3, 1–6. https://doi.org/10.1038/srep02118 http://www.nature.com/srep/2013/130702/srep02118/abs/srep02118.html#supplementary-information

Bondevik, S., Mangerud, J., Birks, H.H., Gulliksen, S., Reimer, P., 2006. Changes in North Atlantic Radiocarbon Reservoir Ages During the Allerød and Younger Dryas. Science (80-.). 312, 1514 LP – 1517. https://doi.org/10.1126/science.1123300

Borchers, B., Marrero, S., Balco, G., Caffee, M., Goehring, B., Lifton, N., Nishiizumi, K., Phillips, F., Schaefer, J., Stone, J., 2016. Geological calibration of spallation production rates in the CRONUS-Earth project. Quat. Geochronol. 31, 188–198. https://doi.org/10.1016/j.quageo.2015.01.009

Bourgois, J., Cisternas, M.E., Braucher, R., Bourlès, D., Frutos, J., 2016. Geomorphic Records along the General Carrera (Chile)–Buenos Aires (Argentina) Glacial Lake (46°–48° S), Climate Inferences, and Glacial Rebound for the Past 7–9 ka. J. Geol. 124, 27–53.

Bradwell, T., Small, D., Fabel, D., Clark, C.D., Chiverrell, R.C., Saher, M.H., Dove, D., Callard, S.L., Burke, M.J., Moreton, S.G., 2019. Pattern, style and timing of British–Irish Ice Sheet retreat: Shetland and northern North Sea sector. J. Quat. Sci.

Briner, J.P., 2011. Dating glacial landforms, in: Singh, V.P., Singh, P., Haritashya, U.K. (Eds.), Encyclopedia of Snow, Ice and Glaciers. Springer, pp. 175–186.

Briner, J.P., Swanson, T.W., Caffee, M., 2001. Late Pleistocene cosmogenic ^{36}Cl glacial chronology of the southwestern Ahklun Mountains, Alaska. Quat. Res. 56, 148–154.

Bronk Ramsey, C., 2013. OxCal 4.2. Web Interface Build.

Bronk Ramsey, C., 2009. Bayesian analysis of radiocarbon dates. Radiocarbon 51, 337–360.

Buck, C.E., Cavanagh, W.G., Litton, C.D., 1996. Bayesian Approach to Interpreting Archaeological Data. Wiley, Chichester.

Burley, D. V, Connaughton, S.P., Clark, G., 2018. Early cessation of ceramic production for ancestral Polynesian society in Tonga. PLoS One 13, e0193166.

Burr, G.S., 2013. RADIOCARBON DATING | Causes of Temporal ^{14}C Variations, in: Elias, S.A., Mock, C.J.B.T.-E. of Q.S. (Second E. (Eds.), Encyclopedia of Quaternary Science: Second Edition. Elsevier, Amsterdam, pp. 336–344. https://doi.org/https://doi.org/10.1016/B978-0-444-53643-3.00046-7

Chevalier, M.-L., Hilley, G., Tapponnier, P., Van Der Woerd, J., Liu-Zeng, J., Finkel, R.C., Ryerson, F.J., Li, H., Liu, X., 2011. Constraints on the late Quaternary glaciations in Tibet from cosmogenic exposure ages of moraine surfaces. Quat. Sci. Rev. 30, 528–554. https://doi.org/http://dx.doi.org/10.1016/j.quascirev.2010.11.005

Chiverrell, R.C., Thrasher, I.M., Thomas, G.S.P., Lang, A., Scourse, J.D., van Landeghem, K.J.J., Mccarroll, D., Clark, C.D., Ó Cofaigh, C., Evans, D.J.A., 2013. Bayesian modelling the retreat of the Irish Sea Ice Stream. J. Quat. Sci. 28, 200–209.

Çiner, A., Sarıkaya, M.A., Yıldırım, C., 2015. Late Pleistocene piedmont glaciations in the Eastern Mediterranean; insights from cosmogenic 36Cl dating of hummocky moraines in southern Turkey. Quat. Sci. Rev. 116, 44–56.

Cockburn, H.A.P., Summerfield, M.A., 2004. Geomorphological applications of cosmogenic isotope analysis. Prog. Phys. Geogr. 28, 1–42. https://doi.org/10.1191/0309133304pp395oa

Codilean, A.T., 2006. Calculation of the cosmogenic nuclide production topographic shielding scaling factor for large areas using DEMs. Earth Surf. Process. Landforms 31, 785–794. https://doi.org/10.1002/esp.1336

Cogez, A., Herman, F., Pelt, É., Reuschlé, T., Morvan, G., Darvill, C.M., Norton, K.P., Christl, M., Märki, L., Chabaux, F., 2018. U-Th and ^{10}Be constraints on sediment recycling in proglacial settings, Lago Buenos Aires, Patagonia. Earth Surf. Dyn. 6, 121–140.

Corbett, L.B., Bierman, P.R., Graly, J.A., Neumann, T.A., Rood, D.H., 2013. Constraining landscape history and glacial erosivity using paired cosmogenic nuclides in Upernavik, northwest Greenland. Geol. Soc. Am. Bull. 125, 1539–1553. https://doi.org/10.1130/b30813.1

Corbett, L.B., Young, N.E., Bierman, P.R., Briner, J.P., Neumann, T.A., Rood, D.H., Graly, J.A., 2011. Paired bedrock and boulder ^{10}Be concentrations resulting from early Holocene ice retreat near Jakobshavn Isfjord, western Greenland. Quat. Sci. Rev. 30, 1739–1749. https://doi.org/http://dx.doi.org/10.1016/j.quascirev.2011.04.001

Curran-Everett, D., Benos, D.J., 2004. Guidelines for reporting statistics in journals published by the American Physiological Society. Am. J. Physiol. 287, C243–C245.

Dalton, A.S., Margold, M., Stokes, C.R., Tarasov, L., Dyke, A.S., Adams, R.S., Allard, S., Arends, H.E., Atkinson, N., Attig, J.W., Barnett, P.J., Barnett, R.L., Batterson, M., Bernatchez, P., Borns, H.W., Breckenridge, A., Briner, J.P., Brouard, E., Campbell, J.E., Carlson, A.E., Clague, J.J., Curry, B.B., Daigneault, R.-A., Dubé-Loubert, H., Easterbrook, D.J., Franzi, D.A., Friedrich, H.G., Funder, S., Gauthier, M.S., Gowan, A.S., Harris, K.L., Hétu, B., Hooyer, T.S., Jennings, C.E., Johnson, M.D., Kehew, A.E., Kelley, S.E., Kerr, D., King, E.L., Kjeldsen, K.K., Knaeble, A.R., Lajeunesse, P., Lakeman, T.R., Lamothe, M., Larson, P., Lavoie, M., Loope, H.M., Lowell, T. V, Lusardi, B.A., Manz, L., McMartin, I., Nixon, F.C., Occhietti, S., Parkhill, M.A., Piper, D.J.W., Pronk, A.G., Richard, P.J.H., Ridge, J.C., Ross, M., Roy, M., Seaman, A., Shaw, J., Stea, R.R., Teller, J.T., Thompson, W.B., Thorleifson, L.H., Utting, D.J., Veillette, J.J., Ward, B.C., Weddle, T.K., Wright, H.E., 2020. An updated radiocarbon-based ice margin chronology for the last deglaciation of the North American Ice Sheet Complex. Quat. Sci. Rev. 234, 106223. https://doi.org/https://doi.org/10.1016/j.quascirev.2020.106223

Darvill, C.M., 2013. Cosmogenic Nuclide Analysis, in: Clarke, L., Nield, J. (Eds.), Geomorphological Techniques. British Society for Geomorphology, London.

Darvill, C.M., Bentley, M.J., Stokes, C.R., Hein, A.S., Rodés, Á., 2015. Extensive MIS 3 glaciation in southernmost Patagonia revealed by cosmogenic nuclide dating of outwash sediments. Earth Planet. Sci. Lett. 429, 157–169.

Darvill, C.M., Menounos, B., Goehring, B.M., Lian, O.B., Caffee, M.W., 2018. Retreat of the western Cordilleran Ice Sheet margin during the last deglaciation. Geophys. Res. Lett. 45, 9710–9720.

Davies, B.J., Darvill, C.M., Lovell, H., Bendle, J.M., Dowdeswell, J.A., Fabel, D., Garcia, J.L., Geiger, A., Glasser, N.F., Gheorghiu, D.M., Harrison, S., Hein, A.S., Martin, J.R.V., Mendelová, M., Palmer, A., Pelto, M.S., Rodes, A., Sagredo, E.A., Smedley, R.K., Smellie, J.L., Thorndycraft, V.R., 2020. The evolution of the Patagonian Ice Sheet from 35 ka to the present day (PATICE). Earth-Science Rev. 204, 103152.

Davies, B.J., Hambrey, M.J., Glasser, N.F., Holt, T., Rodés, A., Smellie, J.L., Carrivick, J.L., Blockley, S.P.E., 2017.

Ice-dammed lateral lake and epishelf lake insights into Holocene dynamics of Marguerite Trough Ice Stream and George VI Ice Shelf, Alexander Island, Antarctic Peninsula. Quat. Sci. Rev. 177. https://doi.org/10.1016/j.quascirev.2017.10.016

Davies, B.J., Hambrey, M.J., Smellie, J.L., Carrivick, J.L., Glasser, N.F., 2012. Antarctic Peninsula Ice Sheet evolution during the Cenozoic Era. Quat. Sci. Rev. 31. https://doi.org/10.1016/j.quascirev.2011.10.012

Davies, B.J., Livingstone, S.J., Roberts, D.H., Evans, D.J.A., Gheorghiu, D.M., Ó Cofaigh, C., 2019. Dynamic ice stream retreat in the central sector of the last British-Irish Ice Sheet. Quat. Sci. Rev. 225, 1–21.

Davies, B.J., Thorndycraft, V.R., Fabel, D., Martin, J.R.V., 2018. Asynchronous glacier dynamics during the Antarctic Cold Reversal in central Patagonia. Quat. Sci. Rev. 200. https://doi.org/10.1016/j.quascirev.2018.09.025

Delunel, R., Bourlès, D.L., van der Beek, P.A., Schlunegger, F., Leya, I., Masarik, J., Paquet, E., 2014. Snow shielding factors for cosmogenic nuclide dating inferred from long-term neutron detector monitoring. Quat. Geochronol. 24, 16–26. https://doi.org/https://doi.org/10.1016/j.quageo.2014.07.003

Denton, G.H., Lowell, T. V, Heusser, C.J., Schlüchter, C., Andersen, B.G., Heusser, L.E., Moreno, P.I., Marchant, D.R., 1999. Geomorphology, Stratigraphy, and Radiocarbon Chronology of LlanquihueDrift in the Area of the Southern Lake District, Seno Reloncaví, and Isla Grande de Chiloé, Chile. Geogr. Ann. Ser. A, Phys. Geogr. 81, 167–229. https://doi.org/10.1111/1468-0459.00057

Desilets, D., Zreda, M., Prabu, T., 2006. Extended scaling factors for in situ cosmogenic nuclides: New measurements at low latitude. Earth Planet. Sci. Lett. 246, 265–276. https://doi.org/https://doi.org/10.1016/j.epsl.2006.03.051

Dong, G., Huang, F., Yi, C., Liu, X., Zhou, W., Caffee, M.W., 2016. Mid-late Pleistocene glacial evolution in the Grove Mountains, East Antarctica, constraints from cosmogenic 10Be surface exposure dating of glacial erratic cobbles. Quat. Sci. Rev. 145, 71–81.

Dortch, J.M., Hughes, P.D., Tomkins, M.D., 2016. Schmidt hammer exposure dating (SHED): Calibration boulder of. Quat. Geochronol. 35, 7e68.

Douglass, D.C., 2007. Constraining boulder erosion rates and ages of mid-Pleistocene moraines, Lago Buenos Aires, Argentina, in: Geological Society of America Abstracts with Programs. p. 65.

Duller, G.A.T., 2008. Single-grain optical dating of Quaternary sediments: why aliquot size matters in luminescence dating. Boreas 37, 589–612.

Duller, G.A.T., 2006. Single grain optical dating of glacigenic deposits. Quat. Geochronol. 1, 296–304.

Dunai, T., 2010. Cosmogenic Nuclides. Principles, concepts and applications in the Earth Surface Sciences. Cambridge University Press, Cambridge.

Dunai, T.J., 2001. Influence of secular variation of the geomagnetic field on production rates of in situ produced cosmogenic nuclides. Earth Planet. Sci. Lett. 193, 197–212.

Dunai, T.J., 2000. Scaling factors for production rates of in situ produced cosmogenic nuclides: a critical reevaluation. Earth Planet. Sci. Lett. 176, 157–169. https://doi.org/http://dx.doi.org/10.1016/S0012-821X(99)00310-6

Dunai, T.J., Lifton, N.A., 2014. The nuts and bolts of cosmogenic nuclide production. Elements 10, 347–350.

Dunai, T.J., Stuart, F.M., 2009. Reporting of cosmogenic nuclide data for exposure age and erosion rate determinations. Quat. Geochronol. 4, 437–440.

Durcan, J.A., King, G.E., Duller, G.A.T., 2015. DRAC: Dose Rate and Age Calculator for trapped charge dating. Quat. Geochronol. 28, 54–61.

Dyke, A.S., Moore, A., Robertson, L., 2003. Deglaciation of North America. Geological Survey of Canada Ottawa, ON.

Ely, J.C., Clark, C.D., Hindmarsh, R.C.A., Hughes, A.L.C., Greenwood, S.L., Bradley, S.L., Gasson, E., Gregoire, L., Gandy, N., Stokes, C.R., 2019. Recent progress on combining geomorphological and geochronological data with ice sheet modelling, demonstrated using the last British–Irish Ice Sheet. J. Quat. Sci.

Espanon, V.R., Honda, M., Chivas, A.R., 2014. Cosmogenic ^{3}He and ^{21}Ne surface exposure dating of young basalts from Southern Mendoza, Argentina. Quat. Geochronol. 19, 76–86.

Fabel, D., Ballantyne, C.K., Xu, S., 2012. Trimlines, blockfields, mountain-top erratics and the vertical dimensions of the last British–Irish Ice Sheet in NW Scotland. Quat. Sci. Rev. 55, 91–102. https://doi.org/10.1016/j.quascirev.2012.09.002

Fabel, D., Small, D., Miguens-Rodriguez, M., Freeman, S.P.H.T., 2010. Cosmogenic nuclide exposure ages from the 'Parallel Roads' of Glen Roy, Scotland. J. Quat. Sci. 25, 597–603. https://doi.org/10.1002/jqs.1318

Fabel, D., Stroeven, A.P., Harbor, J., Kleman, J., Elmore, D., Fink, D., 2002. Landscape preservation under Fennoscandian ice sheets determined from in situ produced 10Be and 26Al. Earth Planet. Sci. Lett. 201, 397–406. https://doi.org/Doi: 10.1016/s0012-821x(02)00714-8

Fairbanks, R.G., Mortlock, R.A., Chiu, T.-C., Cao, L., Kaplan, A., Guilderson, T.P., Fairbanks, T.W., Bloom, A.L., Grootes, P.M., Nadeau, M.-J., 2005. Radiocarbon calibration curve spanning 0 to 50,000 years BP based on paired 230Th/234U/238U and 14C dates on pristine corals. Quat. Sci. Rev. 24, 1781–1796. https://doi.org/https://doi.org/10.1016/j.quascirev.2005.04.007

Fink, D., Smith, A., 2007. An inter-comparison of ^{10}Be and ^{26}Al AMS reference standards and the 10Be half-life. Nucl. Instruments Methods Phys. Res. Sect. B Beam Interact. with Mater. Atoms 259, 600–609.

Foeken, J.P.T., Stuart, F.M., Mark, D.F., 2012. Long-term low latitude cosmogenic ^{3}He production rate determined from a 126 ka basalt from Fogo, Cape Verdes. Earth Planet. Sci. Lett. 359, 14–25.

Frankel, K.L., Finkel, R.C., Owen, L.A., 2010. Terrestrial cosmogenic nuclide geochronology data reporting standards needed. Eos, Trans. Am. Geophys. Union 91, 31–32.

Gandy, N., Gregoire, L.J., Ely, J.C., Cornford, S.L., Clark, C.D., Hodgson, D.M., 2019. Exploring the ingredients required to successfully model the placement, generation, and evolution of ice streams in the British-Irish Ice Sheet. Quat. Sci. Rev. 223, 105915. https://doi.org/https://doi.org/10.1016/j.quascirev.2019.105915

Gillespie, A.R., Bierman, P.R., 1995. Precision of terrestrial exposure ages and erosion rates estimated from

analysis of cosmogenic isotopes produced in situ. J. Geophys. Res. Solid Earth 100, 24637–24649.

Glasser, N.F., Davies, B.J., Carrivick, J.L., Rodés, A., Hambrey, M.J., Smellie, J.L., Domack, E., 2014. Ice-stream initiation, duration and thinning on James Ross Island, northern Antarctic Peninsula. Quat. Sci. Rev. 86. https://doi.org/10.1016/j.quascirev.2013.11.012

Glasser, N.F., Harrison, S., Ivy-Ochs, S., Duller, G.A.T., Kubik, P.W., 2006. Evidence from the Rio Bayo valley on the extent of the North Patagonian Icefield during the Late Pleistocene - Holocene transition. Quat. Res. 65, 70–77. https://doi.org/http://dx.doi.org/10.1016/j.yqres.2005.09.002

Glasser, N.F., Jansson, K.N., Duller, G.A.T., Singarayer, J., Holloway, M., Harrison, S., 2016. Glacial lake drainage in Patagonia (13-8 kyr) and response of the adjacent Pacific Ocean. Sci. Rep. 6, 21064. https://doi.org/10.1038/srep21064 http://www.nature.com/articles/srep21064#supplementary-information

Goehring, B.M., Kurz, M.D., Balco, G., Schaefer, J.M., Licciardi, J., Lifton, N., 2010. A reevaluation of in situ cosmogenic ^{3}He production rates. Quat. Geochronol. 5, 410–418.

Goehring, B.M., Muzikar, P., Lifton, N.A., 2013. An in situ ^{14}C–^{10}Be Bayesian isochron approach for interpreting complex glacial histories. Quat. Geochronol. 15, 61–66. https://doi.org/http://dx.doi.org/10.1016/j.quageo.2012.11.007

Goehring, B.M., Schaefer, J.M., Schluechter, C., Lifton, N.A., Finkel, R.C., Jull, A.J.T., Akçar, N., Alley, R.B., 2011. The Rhone Glacier was smaller than today for most of the Holocene. Geology 39, 679–682.

Golledge, N.R., Menviel, L., Carter, L., Fogwill, C.J., England, M.H., Cortese, G., Levy, R.H., 2014. Antarctic contribution to meltwater pulse 1A from reduced Southern Ocean overturning. Nat. Commun. 5, 5107. https://doi.org/10.1038/ncomms6107

Gosse, J.C., Phillips, F.M., 2001. Terrestrial in situ cosmogenic nuclides: theory and application. Quat. Sci. Rev. 20, 1475–1560. https://doi.org/DOI: 10.1016/S0277-3791(00)00171-2

Graham, A.G.C., Kuhn, G., Meisel, O., Hillenbrand, C.-D., Hodgson, D.A., Ehrmann, W., Wacker, L., Wintersteller, P., dos Santos Ferreira, C., Römer, M., 2017. Major advance of South Georgia glaciers during the Antarctic Cold Reversal following extensive sub-Antarctic glaciation. Nat. Commun. 8, 14798.

Graham, A.G.C., Smith, J.A., 2012. Palaeoglaciology of the Alexander Island ice cap, western Antarctic Peninsula, reconstructed from marine geophysical and core data. Quat. Sci. Rev. 35, 63–81.

Granger, D.E., Lifton, N.A., Willenbring, J.K., 2013. A cosmic trip: 25 years of cosmogenic nuclides in geology. Geol. Soc. Am. Bull. 125, 1379–1402. https://doi.org/10.1130/b30774.1

Granger, D.E., Muzikar, P.F., 2001. Dating sediment burial with in situ-produced cosmogenic nuclides: theory, techniques, and limitations. Earth Planet. Sci. Lett. 188, 269–281.

Guido, Z.S., Ward, D.J., Anderson, R.S., 2007. Pacing the post–Last Glacial Maximum demise of the Animas Valley glacier and the San Juan Mountain ice cap, Colorado. Geology 35, 739–742.

Guilderson, T.P., Reimer, P.J., Brown, T.A., 2005. The Boon and Bane of Radiocarbon Dating. Science (80-.). 307, 362 LP – 364. https://doi.org/10.1126/science.1104164

Hall, B.L., Henderson, G.M., Baroni, C., Kellogg, T.B., 2010. Constant Holocene Southern-Ocean 14C reservoir

ages and ice-shelf flow rates. Earth Planet. Sci. Lett. 296, 115–123.

Harrison, S., Glasser, N.F., Duller, G.A.T., Jansson, K.N., 2012. Early and mid-Holocene age for the Tempanos moraines, Laguna San Rafael, Patagonian Chile. Quat. Sci. Rev. 31, 82–92.

Hatté, C., Jull, A.J.T., 2013. RADIOCARBON DATING | ^{14}C of Plant Macrofossils, in: Elias, S.A., Mock, C.J.B.T.-E. of Q.S. (Second E. (Eds.), . Elsevier, Amsterdam, pp. 361–367. https://doi.org/https://doi.org/10.1016/B978-0-444-53643-3.00049-2

Häuselmann, P., Fiebig, M., Kubik, P.W., Adrian, H., 2007. A first attempt to date the original "Deckenschotter" of Penck and Brückner with cosmogenic nuclides. Quat. Int. 164, 33–42.

Heaton, T.J., Köhler, P., Butzin, M., Bard, E., Reimer, R.W., Austin, W.E.N., Bronk Ramsey, C., Grootes, P.M., Hughen, K.A., Kromer, B., Reimer, P.J., Adkins, J., Burke, A., Cook, M.S., Olsen, J., Skinner, L.C., 2020. Marine20—The Marine Radiocarbon Age Calibration Curve (0–55,000 cal BP). Radiocarbon 62, 779–820. https://doi.org/DOI: 10.1017/RDC.2020.68

Hein, A.S., Cogez, A., Darvill, C.M., Mendelova, M., Kaplan, M.R., Herman, F., Dunai, T.J., Norton, K., Xu, S., Christl, M., 2017. Regional mid-Pleistocene glaciation in central Patagonia. Quat. Sci. Rev. 164, 77–94.

Hein, A.S., Dunai, T.J., Hulton, N.R.J., Xu, S., 2011. Exposure dating outwash gravels to determine the age of the greatest Patagonian glaciations. Geology 39, 103–106. https://doi.org/10.1130/g31215.1

Hein, A.S., Hulton, N.R.J., Dunai, T.J., Schnabel, C., Kaplan, M.R., Naylor, M., Xu, S., 2009. Middle Pleistocene glaciation in Patagonia dated by cosmogenic-nuclide measurements on outwash gravels. Earth Planet. Sci. Lett. 286, 184–197. https://doi.org/http://dx.doi.org/10.1016/j.epsl.2009.06.026

Hein, A.S., Hulton, N.R.J., Dunai, T.J., Sugden, D.E., Kaplan, M.R., Xu, S., 2010. The chronology of the Last Glacial Maximum and deglacial events in central Argentine Patagonia. Quat. Sci. Rev. 29, 1212–1227.

Hein, A.S., Marrero, S.M., Woodward, J., Dunning, S.A., Winter, K., Westoby, M.J., Freeman, S.P.H.T., Shanks, R.P., Sugden, D.E., 2016. Mid-Holocene pulse of thinning in the Weddell Sea sector of the West Antarctic ice sheet. Nat. Commun. 7.

Heroy, D.C., Anderson, J.B., 2007. Radiocarbon constraints on Antarctic Peninsula Ice Sheet retreat following the Last Glacial Maximum (LGM). Quat. Sci. Rev. 26, 3286–3297. https://doi.org/DOI: 10.1016/j.quascirev.2007.07.012

Heyman, J., Applegate, P.J., Blomdin, R., Gribenski, N., Harbor, J.M., Stroeven, A.P., 2016. Boulder height – exposure age relationships from a global glacial 10Be compilation. Quat. Geochronol. 34, 1–11. https://doi.org/https://doi.org/10.1016/j.quageo.2016.03.002

Heyman, J., Stroeven, A.P., Harbor, J.M., Caffee, M.W., 2011. Too young or too old: Evaluating cosmogenic exposure dating based on an analysis of compiled boulder exposure ages. Earth Planet. Sci. Lett. 302, 71–80. https://doi.org/http://dx.doi.org/10.1016/j.epsl.2010.11.040

Hidy, A.J., Gosse, J.C., Pederson, J.L., Mattern, J.P., Finkel, R.C., 2010. A geologically constrained Monte Carlo approach to modeling exposure ages from profiles of cosmogenic nuclides: An example from Lees Ferry, Arizona. Geochemistry, Geophys. Geosystems 11.

Hippe, K., Ivy-Ochs, S., Kober, F., Zasadni, J., Wieler, R., Wacker, L., Kubik, P.W., Schlüchter, C., 2014.

Chronology of Lateglacial ice flow reorganization and deglaciation in the Gotthard Pass area, Central Swiss Alps, based on cosmogenic 10Be and in situ 14C. Quat. Geochronol. 19, 14–26. https://doi.org/https://doi.org/10.1016/j.quageo.2013.03.003

Hjort, C., Ingólfsson, Ó., Möller, P., Lirio, J.M., 1997. Holocene glacial history and sea-level changes on James Ross Island, Antarctic Peninsula. J. Quat. Sci. 12, 259–273. https://doi.org/DOI: 10.1002/(SICI)1099-1417(199707/08)12:4<259::AID-JQS307

Hogg, A.G., Hua, Q., Blackwell, P.G., Niu, M., Buck, C.E., Guilderson, T.P., Heaton, T.J., Palmer, J.G., Reimer, P.J., Reimer, R.W., Turney, C.S.M., Zimmerman, S.R.H., 2013. SHCal13 Southern Hemisphere Calibration, 0–50,000 Years cal BP. Radiocarbon 55, 1889–1903.

Hormes, A., Gjermundsen, E.F., Rasmussen, T.L., 2013. From mountain top to the deep sea – Deglaciation in 4D of the northwestern Barents Sea ice sheet. Quat. Sci. Rev. 75, 78–99. https://doi.org/https://doi.org/10.1016/j.quascirev.2013.04.009

Hughen, K.A., Baillie, M.G.L., Bard, E., Beck, J.W., Bertrand, C.J.H., Blackwell, P.G., Buck, C.E., Burr, G.S., Cutler, K.B., Damon, P.E., Edwards, R.L., Fairbanks, R.G., Friedrich, M., Guilderson, T.P., Kromer, B., McCormac, G., Manning, S., Ramsey, C.B., Reimer, P.J., Reimer, R.W., Remmele, S., Southon, J.R., Stuiver, M., Talamo, S., Taylor, F.W., van der Plicht, J., Weyhenmeyer, C.E., 2004. Marine04 marine radiocarbon age calibration, 0-26 cal kyr BP. Radiocarbon 46, 1059–1086.

Hughes, A.L.C., Greenwood, S.L., Clark, C.D., 2011. Dating constraints on the last British-Irish Ice Sheet: a map and database. J. Maps 7, 156–184.

Hughes, A.L.C., Gyllencreutz, R., Lohne, Ø.S., Mangerud, J., Svendsen, J.I., 2016. The last Eurasian ice sheets–a chronological database and time-slice reconstruction, DATED-1. Boreas 45, 1–45.

Huntley, D.J., Lamothe, M., 2001. Ubiquity of anomalous fading in K-feldspars and hte measurement and correction for it in optical dating. Can. J. Earth Sci. 38, 1093–1106.

Ingólfsson, Ó., 2004. Quaternary glacial and climate history of Antarctica, in: Ehlers, J., Gibbard, P.L. (Eds.), Quaternary Glaciations - Extent and Chronology, Part III, Developments in Quaternary Science. Elsevier, pp. 3–43. https://doi.org/DOI: 10.1016/S1571-0866(04)80109-X

Ivy-Ochs, S., Briner, J.P., 2014. Dating disappearing ice with cosmogenic nuclides. Elements 10, 351–356.

Ivy-Ochs, S., Dühnforth, M., Densmore, A.L., Alfimov, V., 2013. Dating fan deposits with cosmogenic nuclides, in: Dating Torrential Processes on Fans and Cones. Springer, pp. 243–263.

Ivy-Ochs, S., Kober, F., 2007. Cosmogenic nuclides: a versatile tool for studying landscape change during the Quaternary. Quat. Perspect. 160, 134–138.

Jenkins, G.T.H., Duller, G.A.T., Roberts, H.M., Chiverrell, R.C., Glasser, N.F., 2018. A new approach for luminescence dating glaciofluvial deposits-High precision optical dating of cobbles. Quat. Sci. Rev. 192, 263–273.

Johnson, J.S., Bentley, M.J., Smith, J.A., Finkel, R.C., Rood, D.H., Gohl, K., Balco, G., Larter, R.D., Schaefer, J.M., 2014. Rapid Thinning of Pine Island Glacier in the Early Holocene. Science (80-.). 343, 999–1001. https://doi.org/10.1126/science.1247385

Johnson, J.S., Everest, J.D., Leat, P.T., Golledge, N.R., Rood, D.H., Stuart, F.M., 2012. The deglacial history of NW Alexander Island, Antarctica, from surface exposure dating. Quat. Res. 77, 273–280.

Johnson, J.S., Smellie, J.L., Nelson, A.E., Stuart, F.M., 2009. History of the Antarctic Peninsula Ice Sheet since the early Pliocene - Evidence from cosmogenic dating of Pliocene lavas on James Ross Island, Antarctica. Glob. Planet. Change 69, 205–213. https://doi.org/DOI: 10.1016/j.gloplacha.2009.09.001

Jones, R.S., Small, D., Cahill, N., Bentley, M.J., Whitehouse, P.L., 2019. iceTEA: Tools for plotting and analysing cosmogenic-nuclide surface-exposure data from former ice margins. Quat. Geochronol. 51, 72–86. https://doi.org/https://doi.org/10.1016/j.quageo.2019.01.001

Joy, K., Fink, D., Storey, B., Atkins, C., 2014. A 2 million year glacial chronology of the Hatherton Glacier, Antarctica and implications for the size of the East Antarctic Ice Sheet at the Last Glacial Maximum. Quat. Sci. Rev. 83, 46–57. https://doi.org/http://dx.doi.org/10.1016/j.quascirev.2013.10.028

Jull, A.J.T., 2018. Chapter 19 - Geochronology Applied to Glacial Environments, in: Menzies, J., van der Meer, J.J.M. (Eds.), Past Glacial Environments (Second Edition). Elsevier, pp. 665–687. https://doi.org/https://doi.org/10.1016/B978-0-08-100524-8.00020-8

Kaplan, M.R., Douglass, D.C., Singer, B.S., Ackert, R.P., Caffee, M.W., 2005. Cosmogenic nuclide chronology of pre-last glacial maximum moraines at Lago Buenos Aires, 46°S, Argentina. Quat. Res. 63, 301–315. https://doi.org/http://dx.doi.org/10.1016/j.yqres.2004.12.003

Kaplan, M.R., Schaefer, J.M., Strelin, J.A., Denton, G.H., Anderson, R.F., Vandergoes, M.J., Finkel, R.C., Schwartz, R., Travis, S.G., Garcia, J.L., 2016. Patagonian and southern South Atlantic view of Holocene climate. Quat. Sci. Rev. 141, 112–125.

Kaplan, M.R., Strelin, J.A., Schaefer, J.M., Denton, G.H., Finkel, R.C., Schwartz, R., Putnam, A.E., Vandergoes, M.J., Goehring, B.M., Travis, S.G., 2011. In-situ cosmogenic ^{10}Be production rate at Lago Argentino, Patagonia: Implications for late-glacial climate chronology. Earth Planet. Sci. Lett. 309, 21–32. https://doi.org/http://dx.doi.org/10.1016/j.epsl.2011.06.018

Kaplan, M.R., Strelin, J.A., Schaefer, J.M., Peltier, C., Martini, M.A., Flores, E., Winckler, G., Schwartz, R., 2020. Holocene glacier behavior around the northern Antarctic Peninsula and possible causes. Earth Planet. Sci. Lett. 534, 116077.

Kelley, S.E., Kaplan, M.R., Schaefer, J.M., Andersen, B.G., Barrell, D.J.A., Putnam, A.E., Denton, G.H., Schwartz, R., Finkel, R.C., Doughty, A.M., 2014. High-precision ^{10}Be chronology of moraines in the Southern Alps indicates synchronous cooling in Antarctica and New Zealand 42,000 years ago. Earth Planet. Sci. Lett. 405, 194–206.

Kelly, M.A., Lowell, T. V, Hall, B.L., Schaefer, J.M., Finkel, R.C., Goehring, B.M., Alley, R.B., Denton, G.H., 2008. A ^{10}Be chronology of lateglacial and Holocene mountain glaciation in the Scoresby Sund region, east Greenland: implications for seasonality during lateglacial time. Quat. Sci. Rev. 27, 2273–2282.

Kilfeather, A.A., Ó Cofaigh, C., Lloyd, J.M., Dowdeswell, J.A., Xu, S., Moreton, S.G., 2011. Ice-stream retreat and ice-shelf history in Marguerite Trough, Antarctic Peninsula: sedimentological and foraminiferal signatures. Geol. Soc. Am. Bull. 123, 997–1015. https://doi.org/DOI:10.1130/B30282.1

King, G.E., Robinson, R.A.J., Finch, A.A., 2014. Towards successful OSL sampling strategies in glacial

environments: deciphering the influence of depositional processes on bleaching of modern glacial sediments from Jostedalen, Southern Norway. Quat. Sci. Rev. 89, 94–107. https://doi.org/http://dx.doi.org/10.1016/j.quascirev.2014.02.001

Kirkbride, M.P., Winkler, S., 2012. Correlation of Late Quaternary moraines: impact of climate variability, glacier response, and chronological resolution. Quat. Sci. Rev. 46, 1–29. https://doi.org/http://dx.doi.org/10.1016/j.quascirev.2012.04.002

Koffman, T.N.B., Schaefer, J.M., Putnam, A.E., Denton, G.H., Barrell, D.J.A., Rowan, A. V, Finkel, R.C., Rood, D.H., Schwartz, R., Plummer, M.A., Brocklehurst, S.H., 2017. A beryllium-10 chronology of late-glacial moraines in the upper Rakaia valley, Southern Alps, New Zealand supports Southern-Hemisphere warming during the Younger Dryas. Quat. Sci. Rev. 170, 14–25. https://doi.org/https://doi.org/10.1016/j.quascirev.2017.06.012

Kubik, P.W., Christl, M., 2010. ^{10}Be and ^{26}Al measurements at the Zurich 6 MV Tandem AMS facility. Nucl. Instruments Methods Phys. Res. Sect. B Beam Interact. with Mater. Atoms 268, 880–883.

Kubik, P.W., Ivy-Ochs, S., Masarik, J., Frank, M., Schlüchter, C., 1998. ^{10}Be and ^{26}Al production rates deduced from an instantaneous event within the dendro-calibration curve, the landslide of Köfels, Ötz Valley, Austria. Earth Planet. Sci. Lett. 161, 231–241.

Laabs, B.J.C., Munroe, J.S., Best, L.C., Caffee, M.W., 2013. Timing of the last glaciation and subsequent deglaciation in the Ruby Mountains, Great Basin, USA. Earth Planet. Sci. Lett. 361, 16–25.

Laabs, B.J.C., Munroe, J.S., Rosenbaum, J.G., Refsnider, K.A., Mickelson, D.M., Singer, B.S., Caffee, M.W., 2007. Chronology of the last glacial maximum in the upper Bear River basin, Utah. Arctic, Antarct. Alp. Res. 39, 537–548.

Lal, D., 1991. Cosmic ray labeling of erosion surfaces: in situ nuclide production rates and erosion models. Earth Planet. Sci. Lett. 104, 424–439.

Larter, R.D., Anderson, J.B., Graham, A.G.C., Gohl, K., Hillenbrand, C.-D., Jakobsson, M., Johnson, J.S., Kuhn, G., Nitsche, F.O., Smith, J.A., Witus, A.E., Bentley, M.J., Dowdeswell, J.A., Ehrmann, W., Klages, J.P., Lindow, J., Cofaigh, C.Ó., Spiegel, C., 2014. Reconstruction of changes in the Amundsen Sea and Bellingshausen Sea sector of the West Antarctic Ice Sheet since the Last Glacial Maximum. Quat. Sci. Rev. 100, 55–86. https://doi.org/http://dx.doi.org/10.1016/j.quascirev.2013.10.016

Lian, O.B., 2013. LUMINESCENCE DATING | Optical Dating, in: Elias, S.A., Mock, C.J.B.T.-E. of Q.S. (Second E. (Eds.), . Elsevier, Amsterdam, pp. 653–666. https://doi.org/https://doi.org/10.1016/B978-0-444-53643-3.00042-X

Libby, W.F., 1961. Radiocarbon dating. Science (80-.). 133, 621–629.

Libby, W.F., 1955. Radiocarbon Dating (2nd edition). University of Chicago Press, Chicago.

Lifton, N., Sato, T., Dunai, T.J., 2014. Scaling in situ cosmogenic nuclide production rates using analytical approximations to atmospheric cosmic-ray fluxes. Earth Planet. Sci. Lett. 386, 149–160.

Lifton, N., Smart, D.F., Shea, M.A., 2008. Scaling time-integrated in situ cosmogenic nuclide production rates using a continuous geomagnetic model. Earth Planet. Sci. Lett. 268, 190–201.

Lifton, N.A., Bieber, J.W., Clem, J.M., Duldig, M.L., Evenson, P., Humble, J.E., Pyle, R., 2005. Addressing solar modulation and long-term uncertainties in scaling secondary cosmic rays for in situ cosmogenic nuclide applications. Earth Planet. Sci. Lett. 239, 140–161.

Lifton, N.A., Jull, A.J.T., Quade, J., 2001. A new extraction technique and production rate estimate for in situ cosmogenic ^{14}C in quartz. Geochim. Cosmochim. Acta 65, 1953–1969.

Lindow, J., Castex, M., Wittmann, H., Johnson, J.S., Lisker, F., Gohl, K., Spiegel, C., 2014. Glacial retreat in the Amundsen Sea sector, West Antarctica – first cosmogenic evidence from central Pine Island Bay and the Kohler Range. Quat. Sci. Rev. 98, 166–173. https://doi.org/https://doi.org/10.1016/j.quascirev.2014.05.010

Livingstone, S.J., Roberts, D.H., Davies, B.J., Evans, D.J.A., Ó Cofaigh, C., Gheorghiu, D.M., 2015. Late Devensian deglaciation of the Tyne Gap Palaeo-Ice Stream, northern England. J. Quat. Sci. 30. https://doi.org/10.1002/jqs.2813

Lowe, J.J., Walker, M.J.C., 2014. Reconstructing Quaternary Environments. Addison Wesley Longman, London.

Lowe, J.J., Walker, M.J.C., 2000. Radiocarbon dating the last glacial-interglacial transition (^{14}C ka BP) in terrestrial and marine records: the need for new quality assurance protocols. Radiocarbon 42, 53–68.

Luckman, B.H., Masiokas, M.H., Nicolussi, K., 2017. Neoglacial history of Robson Glacier, British Columbia. Can. J. Earth Sci. 54, 1153–1164.

Ludbrook, J., 2008. The presentation of statistics in Clinical and Experimental Pharmacology and Physiology. Clin. Exp. Pharmacol. Physiol. 35, 1271–1274.

Mackintosh, A., White, D., Fink, D., Gore, D.B., Pickard, J., Fanning, P.C., 2007. Exposure ages from mountain dipsticks in Mac. Robertson Land, East Antarctica, indicate little change in ice-sheet thickness since the Last Glacial Maximum. Geology 35, 551–554. https://doi.org/DOI: 10.1130/g23503a.1

Mackintosh, A.N., Anderson, B.M., Pierrehumbert, R.T., 2017. Reconstructing climate from glaciers. Annu. Rev. Earth Planet. Sci. 45, 649–680.

Margold, M., Stokes, C.R., Clark, C.D., 2018. Reconciling records of ice streaming and ice margin retreat to produce a palaeogeographic reconstruction of the deglaciation of the Laurentide Ice Sheet. Quat. Sci. Rev. 189, 1–30.

Marrero, S.M., Phillips, F.M., Borchers, B., Lifton, N., Aumer, R., Balco, G., 2016a. Cosmogenic Nuclide Systematics and the CRONUScalc Program. Quat. Geochronol. 31, 160–187.

Marrero, S.M., Phillips, F.M., Caffee, M.W., Gosse, J.C., 2016b. CRONUS-Earth cosmogenic Cl-36 calibration. Quat. Geochronol. 31, 199–219. https://doi.org/10.1016/j.quageo.2015.10.002

Martin, L.C.P., Blard, P.-H., Balco, G., Lavé, J., Delunel, R., Lifton, N., Laurent, V., 2017. The CREp program and the ICE-D production rate calibration database: A fully parameterizable and updated online tool to compute cosmic-ray exposure ages. Quat. Geochronol. 38, 25–49. https://doi.org/https://doi.org/10.1016/j.quageo.2016.11.006

McCabe, A.M., Clark, P.U., Clark, J., Dunlop, P., 2007. Radiocarbon constraints on readvances of the British-

Irish Ice Sheet in the northern Irish Sea Basin during the last deglaciation. Quat. Sci. Rev. 26, 1204–1211.

McCormac, F.G., Hogg, A.G., Blackwell, P.G., Buck, C.E., Higham, T.F.G., Reimer, P.J., 2004. SHCal04 Southern Hemisphere calibration, 0-11.0 cal kyr BP. Radiocarbon 46, 1087–1092.

McKay, R.M., Dunbar, G.B., Naish, T.R., Barrett, P.J., Carter, L., Harper, M., 2008. Retreat history of the Ross Ice Sheet (Shelf) since the Last Glacial Maximum from deep-basin sediment cores around Ross Island. Palaeogeogr. Palaeoclimatol. Palaeoecol. 260, 245–261. https://doi.org/10.1016/j.palaeo.2007.08.015

Mendelová, M., Hein, A.S., Rodés, Á., Xu, S., 2020. Extensive mountain glaciation in central Patagonia during Marine Isotope Stage 5. Quat. Sci. Rev. 227, 105996.

Miller, G.H., Briner, J.P., Lifton, N.A., Finkel, R.C., 2006. Limited ice-sheet erosion and complex exposure histories derived from in situ cosmogenic ^{10}Be, ^{26}Al, and ^{14}C on Baffin Island, Arctic Canada. Quat. Geochronol. 1, 74–85. https://doi.org/http://dx.doi.org/10.1016/j.quageo.2006.06.011

Moreno, P.I., Denton, G.H., Moreno, H., Lowell, T. V, Putnam, A.E., Kaplan, M.R., 2015. Radiocarbon chronology of the last glacial maximum and its termination in northwestern Patagonia. Quat. Sci. Rev. 122, 233–249.

Murray, A.S., Wintle, A.G., 2000. Luminescence dating of quartz using an improved single-aliquot regenerative-dose protocol. Radiat. Meas. 32, 57–73.

Muscheler, R., Kromer, B., Björck, S., Svensson, A., Friedrich, M., Kaiser, K.F., Southon, J., 2008. Tree rings and ice cores reveal 14C calibration uncertainties during the Younger Dryas. Nat. Geosci. 1, 263–267. https://doi.org/10.1038/ngeo128

Nimick, D.A., McGrath, D., Mahan, S.A., Friesen, B.A., Leidich, J., 2016. Latest Pleistocene and Holocene glacial events in the Colonia valley, Northern Patagonia Icefield, southern Chile. J. Quat. Sci. 31, 551–564.

Nishiizumi, K., 2004. Preparation of ^{26}Al AMS standards. Nucl. Instruments Methods Phys. Res. Sect. B Beam Interact. with Mater. Atoms 223, 388–392.

Nishiizumi, K., Imamura, M., Caffee, M.W., Southon, J.R., Finkel, R.C., McAninch, J., 2007. Absolute calibration of ^{10}Be AMS standards. Nucl. Instruments Methods Phys. Res. Sect. B Beam Interact. with Mater. Atoms 258, 403–413. https://doi.org/https://doi.org/10.1016/j.nimb.2007.01.297

Nishiizumi, K., Winterer, E.L., Kohl, C.P., Klein, J., Middleton, R., Lal, D., Arnold, J.R., 1989. Cosmic ray production rates of ^{10}Be and ^{26}Al in quartz from glacially polished rocks. J. Geophys. Res. Solid Earth 94, 17907–17915.

Ó Cofaigh, C., Davies, B.J., Livingstone, S.J., Smith, J.A., Johnson, J.S., Hocking, E.P., Hodgson, D.A., Anderson, J.B., Bentley, M.J., Canals, M., Domack, E., Dowdeswell, J.A., Evans, J., Glasser, N.F., Hillenbrand, C.-D., Larter, R.D., Roberts, S.J., Simms, A.R., 2014a. Reconstruction of ice-sheet changes in the Antarctic Peninsula since the Last Glacial Maximum. Quat. Sci. Rev. 100, 87–110. https://doi.org/http://dx.doi.org/10.1016/j.quascirev.2014.06.023

Ó Cofaigh, C., Davies, B.J., Livingstone, S.J., Smith, J.A., Johnson, J.S., Hocking, E.P., Hodgson, D.A., Anderson, J.B., Bentley, M.J., Canals, M., Domack, E., Dowdeswell, J.A., Evans, J., Glasser, N.F., Hillenbrand, C.D.,

Larter, R.D., Roberts, S.J., Simms, A.R., 2014b. Reconstruction of ice-sheet changes in the Antarctic Peninsula since the Last Glacial Maximum. Quat. Sci. Rev. 100, 87–110. https://doi.org/10.1016/j.quascirev.2014.06.023

Ó Cofaigh, C., Weilbach, K., Lloyd, J.M., Benetti, S., Callard, S.L., Purcell, C., Chiverrell, R.C., Dunlop, P., Saher, M., Livingstone, S.J., 2019. Early deglaciation of the British-Irish Ice Sheet on the Atlantic shelf northwest of Ireland driven by glacioisostatic depression and high relative sea level. Quat. Sci. Rev. 208, 76–96.

Ortlieb, L., Vargas, G., Saliège, J.-F., 2011. Marine radiocarbon reservoir effect along the northern Chile–southern Peru coast (14–24°S) throughout the Holocene. Quat. Res. 75, 91–103. https://doi.org/http://dx.doi.org/10.1016/j.yqres.2010.07.018

Patton, H., Hubbard, A., Andreassen, K., Auriac, A., Whitehouse, P.L., Stroeven, A.P., Shackleton, C., Winsborrow, M., Heyman, J., Hall, A.M., 2017. Deglaciation of the Eurasian ice sheet complex. Quat. Sci. Rev. 169, 148–172. https://doi.org/https://doi.org/10.1016/j.quascirev.2017.05.019

Patton, H., Hubbard, A., Andreassen, K., Winsborrow, M., Stroeven, A.P., 2016. The build-up, configuration, and dynamical sensitivity of the Eurasian ice-sheet complex to Late Weichselian climatic and oceanic forcing. Quat. Sci. Rev. 153, 97–121. https://doi.org/http://dx.doi.org/10.1016/j.quascirev.2016.10.009

Phillips, F.M., Argento, D.C., Balco, G., Caffee, M.W., Clem, J., Dunai, T.J., Finkel, R., Goehring, B., Gosse, J.C., Hudson, A.M., Jull, A.J.T., Kelly, M.A., Kurz, M., Lal, D., Lifton, N., Marrero, S.M., Nishiizumi, K., Reedy, R.C., Schaefer, J., Stone, J.O.H., Swanson, T., Zreda, M.G., 2016. The CRONUS-Earth Project: A synthesis. Quat. Geochronol. 31, 119–154. https://doi.org/10.1016/j.quageo.2015.09.006

Portenga, E.W., Bierman, P.R., 2011. Understanding Earth's eroding surface with 10 Be. GSA today 21, 4–10.

Portenga, E.W., Bierman, P.R., Rizzo, D.M., Rood, D.H., 2013. Low rates of bedrock outcrop erosion in the central Appalachian Mountains inferred from in situ ^{10}Be. GSA Bull. 125, 201–215.

Porter, S.C., 2005. Pleistocene snowlines and glaciation of the Hawaiian Islands. Quat. Int. 138–139, 118–128.

Pudsey, C.J., Murray, J.W., Appleby, P., Evans, J., 2006. Ice shelf history from petrographic and foraminiferal evidence, Northeast Antarctic Peninsula. Quat. Sci. Rev. 25, 2357–2379. https://doi.org/DOI: 10.1016/j.quascirev.2006.01.029

Putkonen, J., Swanson, T., 2003. Accuracy of cosmogenic ages for moraines. Quat. Res. 59, 255–261. https://doi.org/http://dx.doi.org/10.1016/S0033-5894(03)00006-1

Putnam, A.E., Schaefer, J.M., Barrell, D.J.A., Vandergoes, M., Denton, G.H., Kaplan, M.R., Finkel, R.C., Schwartz, R., Goehring, B.M., Kelley, S.E., 2010. In situ cosmogenic ^{10}Be production-rate calibration from the Southern Alps, New Zealand. Quat. Geochronol. 5, 392–409.

Putnam, A.E., Schaefer, J.M., Denton, G.H., Barrell, D.J.A., Birkel, S.D., Andersen, B.G., Kaplan, M.R., Finkel, R.C., Schwartz, R., Doughty, A.M., 2013. The Last Glacial Maximum at 44°S documented by a 10Be moraine chronology at Lake Ohau, Southern Alps of New Zealand. Quat. Sci. Rev. 62, 114–141. https://doi.org/http://dx.doi.org/10.1016/j.quascirev.2012.10.034

Reimer, P.J., Austin, W.E.N., Bard, E., Bayliss, A., Blackwell, P.G., Bronk Ramsey, C., Butzin, M., Cheng, H.,

Edwards, R.L., Friedrich, M., Grootes, P.M., Guilderson, T.P., Hajdas, I., Heaton, T.J., Hogg, A.G., Hughen, K.A., Kromer, B., Manning, S.W., Muscheler, R., Palmer, J.G., Pearson, C., van der Plicht, J., Reimer, R.W., Richards, D.A., Scott, E.M., Southon, J.R., Turney, C.S.M., Wacker, L., Adolphi, F., Büntgen, U., Capano, M., Fahrni, S.M., Fogtmann-Schulz, A., Friedrich, R., Köhler, P., Kudsk, S., Miyake, F., Olsen, J., Reinig, F., Sakamoto, M., Sookdeo, A., Talamo, S., 2020. THE INTCAL20 NORTHERN HEMISPHERE RADIOCARBON AGE CALIBRATION CURVE (0–55 CAL kBP). Radiocarbon 1–33. https://doi.org/DOI: 10.1017/RDC.2020.41

Reimer, P.J., Baillie, M.G.L., Bard, E., Bayliss, A., Beck, J.W., Blackwell, P.G., Ramsey, C.B., Buck, C.E., Burr, G.S., Edwards, R.L., Friedrich, M., Grootes, P.M., Guilderson, T.P., Hajdas, I., Heaton, T.J., Hogg, A.G., Hughen, K.A., Kaiser, K.F., Kromer, B., McCormac, F.G., Manning, S.W., Reimer, R.W., Richards, D.A., Southon, J.R., Talamo, S., Turney, C.S.M., van der Plicht, J., Weyhenmeye, C.E., 2009. INTCAL09 and MARINE09 radiocarbon age calibration curves, 0-50,000 years cal BP. Radiocarbon 51, 1111–1150.

Reimer, P.J., Bard, E., Bayliss, A., Beck, J.W., Blackwell, P.G., Ramsey, C.B., Buck, C.E., Cheng, H., Edwards, R.L., Friedrich, M., 2013. IntCal13 and Marine13 radiocarbon age calibration curves 0–50,000 years cal BP. Radiocarbon 55, 1869–1887.

Reimer, P.J., Reimer, R.W., 2001. A Marine Reservoir Correction Database and On-Line Interface. Radiocarbon 43, 461–463. https://doi.org/DOI: 10.1017/S0033822200038339

Repka, J.L., Anderson, R.S., Finkel, R.C., 1997. Cosmogenic dating of fluvial terraces, Fremont River, Utah. Earth Planet. Sci. Lett. 152, 59–73.

Reusche, M., Winsor, K., Carlson, A.E., Marcott, S.A., Rood, D.H., Novak, A., Roof, S., Retelle, M., Werner, A., Caffee, M., Clark, P.U., 2014. ^{10}Be surface exposure ages on the late-Pleistocene and Holocene history of Linnébreen on Svalbard. Quat. Sci. Rev. 89, 5–12. https://doi.org/https://doi.org/10.1016/j.quascirev.2014.01.017

Reynhout, S., Sagredo, E.A., Kaplan, M.R., Aravena, J.C., Martini, M.A., Moreno, P.I., Rojas, M., Schwartz, R., Schaefer, J.M., 2019. Holocene glacier fluctuations in Patagonia are modulated by summer insolation intensity and paced by Southern Annular Mode-like variability. Quat. Sci. Rev. in press.

Rhodes, E.J., 2011. Optically stimulated luminescence dating of sediments over the past 200,000 years. Annu. Rev. Earth Planet. Sci. 39, 461–488.

Rinterknecht, V.R., Bitinas, A., Clark, P.U., Raisbeck, G.M., Yiou, F., Brook, E.J., 2008. Timing of the last deglaciation in Lithuania. Boreas 37, 426–433. https://doi.org/10.1111/j.1502-3885.2008.00027.x

Rinterknecht, V.R., Clark, P.U., Raisbeck, G.M., Yiou, F., Bitinas, A., Brook, E.J., Marks, L., Zelčs, V., Lunkka, J.-P., Pavlovskaya, I.E., 2006. The last deglaciation of the southeastern sector of the Scandinavian Ice Sheet. Science (80-.). 311, 1449–1452.

Sagredo, E.A., Kaplan, M.R., Araya, P.S., Lowell, T. V, Aravena, J.C., Moreno, P.I., Kelly, M.A., Schaefer, J.M., 2018. Trans-pacific glacial response to the Antarctic Cold Reversal in the southern mid-latitudes. Quat. Sci. Rev. 188, 160–166. https://doi.org/https://doi.org/10.1016/j.quascirev.2018.01.011

Sarıkaya, M.A., Çiner, A., Yıldırım, C., 2017. Cosmogenic ^{36}Cl glacial chronologies of the Late Quaternary glaciers on Mount Geyikdağ in the Eastern Mediterranean. Quat. Geochronol. 39, 189–204.

Schaefer, J.M., Denton, G.H., Kaplan, M., Putnam, A., Finkel, R.C., Barrell, D.J.A., Andersen, B.G., Schwartz, R., Mackintosh, A., Chinn, T., SchlÃ¼chter, C., 2009. High-Frequency Holocene Glacier Fluctuations in New Zealand Differ from the Northern Signature. Science (80-.). 324, 622–625. https://doi.org/10.1126/science.1169312

Schildgen, T.F., Phillips, W.M., Purves, R.S., 2005. Simulation of snow shielding corrections for cosmogenic nuclide surface exposure studies. Geomorphology 64, 67–85. https://doi.org/https://doi.org/10.1016/j.geomorph.2004.05.003

Schimmelpfennig, I., Benedetti, L., Finkel, R., Pik, R., Blard, P.-H., Bourlès, D., Burnard, P., Williams, A., 2009. Sources of in-situ ^{36}Cl in basaltic rocks. Implications for calibration of production rates. Quat. Geochronol. 4, 441–461. https://doi.org/10.1016/j.quageo.2009.06.003

Schimmelpfennig, I., Schaefer, J.M., Akçar, N., Koffman, T., Ivy-Ochs, S., Schwartz, R., Finkel, R.C., Zimmerman, S., Schlüchter, C., 2014. A chronology of Holocene and Little Ice Age glacier culminations of the Steingletscher, Central Alps, Switzerland, based on high-sensitivity beryllium-10 moraine dating. Earth Planet. Sci. Lett. 393, 220–230.

Simms, A.R., Milliken, K.T., Anderson, J.B., Wellner, J.S., 2011. The marine record of deglaciation of the South Shetland Islands, Antarctica since the Last Glacial Maximum. Quat. Sci. Rev. 30, 1583–1601.

Singer, B.S., Ackert, R.P., Guillou, H., 2004a. ^{40}Ar/^{39}Ar and K-Ar chronology of Pleistocene glaciations in Patagonia. Geol. Soc. Am. Bull. 116, 434–450.

Singer, B.S., Brown, L.L., Rabassa, J.O., Guillou, H., 2004b. ^{40}Ar/^{39}Ar chronology of late Pliocene and Early Pleistocene geomagnetic and glacial events in southern Argentina. Timescales Paleomagn. F. 175–190.

Small, D., Bentley, M.J., Jones, R.S., Pittard, M.L., Whitehouse, P.L., 2019. Antarctic ice sheet palaeo-thinning rates from vertical transects of cosmogenic exposure ages. Quat. Sci. Rev. 206, 65–80. https://doi.org/https://doi.org/10.1016/j.quascirev.2018.12.024

Small, D., Clark, C.D., Chiverrell, R.C., Smedley, R.K., Bateman, M.D., Duller, G.A.T., Ely, J.C., Fabel, D., Medialdea, A., Moreton, S.G., 2017. Devising quality assurance procedures for assessment of legacy geochronological data relating to deglaciation of the last British-Irish Ice Sheet. Earth-Science Rev. 164, 232–250. https://doi.org/https://doi.org/10.1016/j.earscirev.2016.11.007

Small, D., Fabel, D., 2015. A Lateglacial ^{10}Be production rate from glacial lake shorelines in Scotland. J. Quat. Sci. 30, 509–513.

Smedley, R.K., 2018. Telling the time with dust, sand and rocks. Elem. An Int. Mag. Mineral. Geochemistry, Petrol. 14, 9–14.

Smedley, R.K., Buylaert, J.-P., Ujvari, G., 2019. Comparing the accuracy and precision of luminescence ages for partially-bleached sediments using single grains of K-feldspar and quartz. Quat. Geochronol. 53, 101007.

Smedley, R.K., Glasser, N.F., Duller, G.A.T., 2016. Luminescence dating of glacial advances at Lago Buenos Aires (~ 46° S), Patagonia. Quat. Sci. Rev. 134, 59–73.

Smedley, R.K., Pearce, N.J.G., 2016. Internal U, Th and Rb concentrations of alkali-feldspar grains: Implications for luminescence dating. Quat. Geochronol. 35, 16–25.

Smedley, R.K., Skirrow, G.K.A., 2020. Luminescence Dating in Fluvial Settings: Overcoming the Challenge of Partial Bleaching, in: Palaeohydrology. Springer, pp. 155–168.

Smith, J.A., Hillenbrand, C.-D., Kuhn, G., Klages, J.P., Graham, A.G.C., Larter, R.D., Ehrmann, W., Moreton, S.G., Wiers, S., Frederichs, T., 2014. New constraints on the timing of West Antarctic Ice Sheet retreat in the eastern Amundsen Sea since the Last Glacial Maximum. Glob. Planet. Change 122, 224–237.

Sohbati, R., Murray, A.S., Buylaert, J., Almeida, N.A.C., Cunha, P.P., 2012. Optically stimulated luminescence (OSL) dating of quartzite cobbles from the T apada do M ontinho archaeological site (east-central P ortugal). Boreas 41, 452–462.

Spencer, C.J., Yakymchuk, C., Ghaznavi, M., 2017. Visualising data distributions with kernel density estimation and reduced chi-squared statistic. Geosci. Front. 8, 1247–1252. https://doi.org/https://doi.org/10.1016/j.gsf.2017.05.002

Sterken, M., Roberts, S.J., Hodgson, D.A., Vyverman, W., Balbo, A.L., Sabbe, K., Moreton, S.G., Verleyen, E., 2012. Holocene glacial and climate history of Prince Gustav Channel, northeastern Antarctic Peninsula. Quat. Sci. Rev. 31, 93–111.

Stokes, C.R., Tarasov, L., 2010. Ice streaming in the Laurentide Ice Sheet: A first comparison between data-calibrated numerical model output and geological evidence. Geophys. Res. Lett. 37, L01501. https://doi.org/10.1029/2009gl040990

Stokes, S., 1999. Luminescence dating applications in geomorphological research. Geomorphology 29, 153–171.

Stone, J.O., 2000. Air pressure and cosmogenic isotope production. J. Geophys. Res. 105, 23753–23759.

Stone, J.O., Balco, G.A., Sugden, D.E., Caffee, M.W., Sass, L.C., Cowdery, S.G., Siddoway, C., 2003. Holocene deglaciation of Marie Byrd Land, West Antarctica. Science (80-.). 299, 99–102.

Strelin, J.A., Denton, G.H., Vandergoes, M.J., Ninnemann, U.S., Putnam, A.E., 2011. Radiocarbon chronology of the late-glacial Puerto Bandera moraines, southern Patagonian Icefield, Argentina. Quat. Sci. Rev. 30, 2551–2569.

Stroeven, A.P., Fabel, D., Hättestrand, C., Harbor, J., 2002. A relict landscape in the centre of Fennoscandian glaciation: cosmogenic radionuclide evidence of tors preserved through multiple glacial cycles. Geomorphology 44, 145–154.

Stroeven, A.P., Heyman, J., Fabel, D., Björck, S., Caffee, M.W., Fredin, O., Harbor, J.M., 2015. A new Scandinavian reference 10Be production rate. Quat. Geochronol. 29, 104–115.

Stuiver, M., Braziunas, T.F., 1993. Modeling atmospheric ^{14}C influences and ^{14}C ages of marine samples to 10,000 BC. Radiocarbon 35, 137–189.

Stuiver, M., Reimer, P.J., Reimer, R.W., 2009. CALIB 5.0.1. Program and Documentation. http://www.calib.qub.ac.uk/.

Sugden, D.E., Balco, G., Cowdery, S.G., Stone, J.O., Sass Iii, L.C., 2005. Selective glacial erosion and weathering zones in the coastal mountains of Marie Byrd Land, Antarctica. Geomorphology 67, 317–334.

Thomsen, K.J., Murray, A.S., Jain, M., 2011. Stability of IRSL signals from sedimentary K-feldspar samples. Geochronometria 38, 1–13.

Thomsen, K.J., Murray, A.S., Jain, M., Bøtter-Jensen, L., 2008. Laboratory fading rates of various luminescence signals from feldspar-rich sediment extracts. Radiat. Meas. 43, 1474–1486.

Thorndycraft, V.R., Bendle, J.M., Benito, G., Davies, B.J., Sancho, C., Palmer, A.P., Fabel, D., Medialdea, A., Martin, J.R. V, 2019. Glacial lake evolution and Atlantic-Pacific drainage reversals during deglaciation of the Patagonian Ice Sheet. Quat. Sci. Rev. 203, 102–127. https://doi.org/https://doi.org/10.1016/j.quascirev.2018.10.036

Turrin, B.D., Muffler, L.J.P., Clynne, M.A., Champion, D.E., 2007. Robust 24±6 ka 40Ar/39Ar age of a low-potassium tholeiitic basalt in the Lassen region of NE California. Quat. Res. 68, 96–110. https://doi.org/https://doi.org/10.1016/j.yqres.2007.02.004

Verleyen, E., Hodgson, D.A., Sabbe, K., Cremer, H., Emslie, S.D., Gibson, J., Hall, B., Imura, S., Kudoh, S., Marshall, G.J., McMinn, A., Melles, M., Newman, L., Roberts, D., Roberts, S.J., Singh, S.M., Sterken, M., Tavernier, I., Verkulich, S., de Vyver, E. Van, Van Nieuwenhuyze, W., Wagner, B., Vyverman, W., 2011. Post-glacial regional climate variability along the East Antarctic coastal margin - Evidence from shallow marine and coastal terrestrial records. Earth-Science Rev. 104, 199–212. https://doi.org/doi: 10.1016/j.earscirev.2010.10.006

White, D., Fülöp, R.-H., Bishop, P., Mackintosh, A., Cook, G., 2011. Can in-situ cosmogenic 14C be used to assess the influence of clast recycling on exposure dating of ice retreat in Antarctica? Quat. Geochronol. 6, 289–294. https://doi.org/https://doi.org/10.1016/j.quageo.2011.03.004

Wijbrans, J.R., Kuiper, K.F., 2013. K/AR AND ^{40}AR/^{39}AR DATING, in: Elias, S.A., Mock, C.J.B.T.-E. of Q.S. (Second E. (Eds.), . Elsevier, Amsterdam, pp. 477–482. https://doi.org/https://doi.org/10.1016/B978-0-444-53643-3.00040-6